NJC

PAPER

View Article Online
View Journal | View Issue

Cite this: *New J. Chem.*, 2026, **50**, 6873

# A naphthalene-based and hydroxyamide-functionalized hybrid Schiff base and its dimeric and dinuclear Zn(II) complex: synthesis, structural and theoretical characterization, and optical, DPPH scavenging and *in silico* ADME properties

Özlem Güngör, *[a] Gaurav Jhaa [b] and Savaş Kaya [c]

Received 9th February 2026,
Accepted 12th March 2026

DOI: 10.1039/d6nj00512h

rsc.li/njc

A novel hybrid ligand **2b** (3,5-bis((*E*)-((2-hydroxynaphthalen-1-yl)methylene)amino)-*N*-(2-hydroxyphenyl)-benzamide) was obtained from the amidation reaction between Schiff base **1b** (3,5-bis((*E*)-((2-hydroxynaphthalen-1-yl)methylene)amino)benzoic acid) and 2-hydroxyaniline by using dicyclohexyl-carbodiimide. The coordination of **2b** with zinc ions resulted in the formation of a neutral dinuclear and non-electrolyte complex of **3b** $[Zn_2L_2(H_2O)_4]\cdot 2H_2O$ at a stoichiometric 2 : 2 mol ratio, where each zinc(II) cation is six-coordinate in a distorted octahedral geometry with two coordinated water molecules. They were characterized by IR, NMR and UV-vis spectroscopy both experimentally and theoretically. Thermal and mass analyses provided information regarding the presence of water molecules. DFT simulations were performed to obtain the lowest-energy structures of the compounds. The calculated frontier molecular orbital gaps correlated well with the optical bandgaps. **1b–2b** emitted strong greenish-blue and green emissions in dilute DMSO and DMF solutions. The emission color of **3b** shifted to bluish-green/green. Their emission properties were evaluated in binary aqueous mixtures with varying water content ($f_w$ = 0–90%). Upon increasing the water fraction, the intensity was enhanced by changing the spectral profiles of the media. **1b–3b** possess lower DPPH scavenging activity than ascorbic acid. The absorption, distribution, metabolism, and elimination (ADME) parameters were calculated for the ligands.

## Introduction

Zinc(II) complexes are the most commonly investigated metal–organic frameworks (MOFs) because of the possibility of having a wide variety of coordination arrangements resulting from the $d^{10}$ electronic configuration. These complexes exhibit promising functional properties owing to the combination of the advantages of both metal ions and organic ligands. Many zinc complexes emit in the range of blue-green to red emission of the electromagnetic spectrum for application in photo- and electroluminescent materials.[1,2] In the area of photochemistry, the fluorescence emission of luminophores can be hampered upon aggregation in high concentration solution, which is known as the 'aggregation-caused quenching (ACQ)' effect, due to the existence of π–π stacking interaction between the independent molecules.[3–5] Aggregation-induced emission (AIE) materials display weak or almost no fluorescence in dilute solutions, but exhibit enhanced fluorescence intensity in the solid state or aggregated state.[6,7] On the other hand, metal complexes can exhibit better fluorescence performance than the corresponding ligands because of their high photo- and thermal stabilities.[8]

Schiff bases with imine/azomethine groups are an important branch of inorganic multidentate ligands. The 2-hydroxy Schiff bases obtained by the condensation of salicylaldehyde/2-hydroxy-1-naphthylaldehyde with aromatic amines are phenol (OH) and keto (NH) tautomers in the crystalline state and solution.[9] The NH tautomer can also exist in zwitterionic form.[10] The phototautomerization from enol to keto tautomer is connected to an intramolecular proton transfer (IPT) reaction in a six-membered chelate ring between the phenolic oxygen and imine nitrogen atoms, which requires a small amount of energy. Energy can be obtained by light or temperature changes, causing these Schiff bases to exhibit photochromic and thermochromic behaviors.[11] Amido-linked Schiff bases

---

[a] Department of Chemistry, Faculty of Science, Gazi University, 06500 Ankara, Turkey. E-mail: ozlemgungor@gazi.edu.tr
[b] Department of Chemical Sciences, Indian Institute of Science Education and Research Mohali (IISER Mohali), Punjab, 140306, India. E-mail: gauravjhaa@iisermohali.ac.in
[c] Department of Chemistry, Faculty of Science, Sivas Cumhuriyet University, Sivas, 58140, Turkey. E-mail: savaskaya@cumhuriyet.edu.tr

consisting of imine (C═N) and amide (C(O)–N) functional groups are among the well-known classes of chelating ligands used in coordination chemistry to obtain new transition metal complexes. They are routinely produced by reacting hydrazides/hydrazones with aldehydes/ketones.[12] A number of these compounds are of interest for use in fluorometric and colorimetric sensing of metal ions[13,14] or inorganic anions.[15] Such complexes have been reported to have potential industrial applications in the disciplines of supramolecular chemistry, corrosion,[16] and catalysis,[17] as well as pharmacological activities, including antimicrobial, antioxidant, and anticancer activities.[18,19]

This study focused on combining and improving the properties of Schiff bases and amides in the structure of one molecule, which is one of the most promising scaffolds in the field of biology and a promising class of fluorescent materials. Moreover, the amide (C═O) bond may be a key functional group in the formation of intermolecular hydrogen-bonded aggregates for fundamental photochemistry studies. This paper reports the synthesis and characterization of a new hydroxyamide-functionalized Schiff base (**2b**) and its zinc complex (**3b**) for potential medicinal and optoelectronic applications in the future. *N*,*N′*-Dicyclohexylcarbodiimide has been utilized in the acylation of the carboxyl group of the diimine-Schiff base (**1b**) for the condensation of 2-hydroxyaniline. A dimeric Zn(II) complex (**3b**) was synthesized in a 2 : 2 (L : M) ratio, in which **2b** behaves as a deprotonated $O_2N_2$ tetradentate ligand and binds to metal cations using naphtholic oxygen and imine nitrogen atoms. A dinuclear complex consisting of two Zn(II) ions indicates that each zinc centre is surrounded by NO donor atoms of two ligands and two water molecules, resulting in a distorted octahedral geometry. Such bridging modes with zinc(II) complexes have been published rarely in the literature, and this is suggested to be the first investigation related to amido-Schiff base ligands. Their structures were identified *via* IR, NMR, mass, and UV-vis spectroscopies, elemental analysis, and density functional theory (DFT) calculations. **3b** exhibited good thermal stability in the solid state. The IPT and chromaticity characteristics of the compounds were investigated in DMSO and DMF solutions using UV-vis and fluorescence spectrometry. These synthesized compounds act as ACQ active molecules in highly concentrated solutions, whereas they are AIE-fluorophores in a solvent/$H_2O$ mixture. They have also been evaluated for their antioxidant properties in DMSO using the DPPH assay. Theoretical absorption, distribution, metabolism, and elimination (ADME) parameters were calculated *in silico* for **1b** and **2b**.

The molecular framework of the new hybrid Schiff base **2b** was designed to incorporate an extended π-conjugated system composed of phenyl and naphthyl rings together with potential hydrogen-bonding sites, which are expected to stabilize a more rigid molecular conformation. This electronic modification may lead to noticeable shifts in emission wavelengths. Based on the structural features, it is anticipated that the IPT process in the excited-state will play an important role in determining whether this amido-Schiff base exhibits ACQ or AIE characteristics in solution and in the aggregated state. Complexation with $Zn^{2+}$ ions is expected to rigidify the molecular framework through chelation involving the imine nitrogen and hydroxyl oxygen atoms. This coordination restricts intramolecular motions and minimizes non-radiative decay pathways, giving rise to chelation-enhanced fluorescence (CHEF). In combination with aggregation-induced restriction, this effect may lead to a synergistic enhancement of fluorescence intensity. The molecular design of the amido-Schiff base also suggests a plausible mechanism for radical scavenging activity. The conjugated π-system formed by the naphthyl and phenyl rings enables efficient delocalization of unpaired electrons, thereby stabilizing radical intermediates, while the phenolic and naphtholic OH groups can donate hydrogen atoms to neutralize reactive radicals. Consequently, this compound represents a suitable candidate for antioxidant evaluation using the DPPH assay. Furthermore, the presence of a conjugated amide group may favorably influence the ADME properties, potentially improving the balance between solubility and lipophilicity as well as metabolic stability, which may enhance bioavailability. The hydrogen-bonding capability of the molecule may also affect protein binding and tissue distribution, contributing to a potentially favorable pharmacokinetic profile. In summary, the rational design of the hybrid Schiff base **2b** and zinc complex **3b** integrates three key aspects:

(i) Structure–photophysical relationship governing the ACQ-to-AIE transition,

(ii) Metal coordination effects enhancing fluorescence through the CHEF mechanism,

(iii) Structure–activity relationships associated with potential antioxidant and ADME properties.

# Experimental

### Materials and instrumentation

3,5-Diaminobenzoic acid (Aldrich), 2-hydroxy-1-naphthaldehyde (Aldrich), *N*,*N′*-dicyclohexylcarbodiimide (DCC) (Sigma-Aldrich), 2-hydroxyaniline (Aldrich), zinc nitrate hexahydrate ($Zn(NO_3)_2 \cdot 6H_2O$) (Acros Organics), L-ascorbic acid (Carlo Erba), and 1,1-diphenyl-2-picrylhydrazyl (DPPH) (Aldrich) were used as received. Absolute ethyl alcohol (EtOH) (Sigma-Aldrich), dichloromethane (DCM) (Riedel-de-Haen), dimethyl sulfoxide (DMSO) (Merck), and *N*,*N*-dimethylformamide (DMF) (Riedel-de-Haen) were of spectroscopic purity.

Melting points were determined using a Stuart SMP30 apparatus and uncorrected. Carbon, hydrogen, and nitrogen microanalyses were performed using a Thermo Scientific Flash 2000 elemental analyzer. Infrared absorption (ATR) spectra were recorded at room temperature in the wavenumber range from 4000 to 400 $cm^{-1}$ using a Thermo Scientific Nicolet iD5 spectrometer as a powder, at a resolution of 4 $cm^{-1}$ accumulating 20 scans per spectrum, supplied by OMNIC software. Nuclear magnetic resonance (NMR) spectra were established in deutero dimethylsulfoxide on a Bruker Avance Neo spectrometer (500 MHz), operating at 500.13 MHz ($^1$H) and 125.75 MHz ($^{13}$C), employing $Me_4Si$ (TMS) as an internal standard (abbreviations: s, singlet; d, doublet; t, triplet). Typical spectral parameters were utilized for $^1$H-NMR: spectral width 11.90–12.50 kHz, per point digital resolution 0.363–0.381 Hz, acquisition time 2.62–2.75 s, relaxation delay 1 s, pulse width 8.00–8.64 μs, temperature 296.1 ± 0.1 K; for $^{13}$C-NMR: spectral width 30.12 kHz, per point digital resolution 0.919 Hz, acquisition time 1.08 s, relaxation delay 2 s, pulse width 10 μs, temperature 299.2 ± 0.3 K. The high resolution mass spectrum (HRMS) was recorded on an Agilent LC Q-TOF mass spectrometer at high cone voltage (150.0 V) using electrospray (ESI) positive ionization mode. All the solutions were prepared in methanol and subjected to spectrometry. An acetonitrile-water mixture containing 0.1% formic acid was used as the mobile phase. The conductivity was measured in DMSO solvent ($C = 1.0 \times 10^{-3}$ M) on a Bante Instrument 950 conductivity meter equipped with a DJS-0.1 conductivity electrode. TGA-DTA thermograms were collected on a SII7300 ExstarDTA instrument under a nitrogen atmosphere within the range of 25–750 °C and under an $O_2$ atmosphere between 750 and 800 °C at a heating rate of 10 °C min$^{-1}$. Ultraviolet-visible (UV-vis) absorption spectra were captured in DMSO and DMF ($C$ = 100 and 50 μM) with quartz cuvettes of 1 cm path length in the 250–900 nm range on an Analytik Jena Specord 200 spectrophotometer (slit 1 nm, lamp change at 300, $\Delta\lambda$ 1 nm, speed 50 nm s$^{-1}$). The purity of the compounds was determined using thin-layer chromatography (TLC, silica gel $F_{254}$).

## Synthesis

**Compound 1b [3,5-bis((*E*)-((2-hydroxynaphthalen-1-yl)methylene)amino)benzoic acid].** Diimine-Schiff base was synthesized according to a previously reported procedure.[20] 3,5-Diaminobenzoic acid (5 mmol) was dissolved in absolute ethanol (50 mL) with stirring and heating. A red-colored solution of 2-hydroxy-1-naphthaldehyde (10 mmol) in EtOH (40 mL) was slowly added to a light-yellow solution of amine. The color of the solution initially turned yellow and then orange. The resulting dark orange mixture was refluxed for 3 h with stirring. After cooling to room temperature, the resulting solid was filtered and dried in air. It was purified by crystallization in absolute ethanol. Orange solid, yield: 84%, decomposition point: 233 °C. IR (ATR, $\nu$ (cm$^{-1}$)): 3053 (Ar–H), 2870 (C–H), 2763 (O–H, carboxyl), 2502 (O–H, naphthol), 1702 (C═O), 1620 (C═N), 1587/1527 (C═C), 1492, 1469, 1446, 1418, 1405, 1351, 1301 (C–O, carboxyl), 1254, 1221, 1203 (C–O, naphthol), 1135 (C–N). $^1$H NMR (500 MHz, DMSO-$d_6$, $\delta$ (ppm)): 7.071–7.089 (d, $J$ = 9.164 Hz, 2H, Ar–H), 7.285 (s, 1H, Ar–H), 7.375–7.404 (t, $J$ = 7.133 Hz, 2H, Ar–H), 7.572–7.605 (t-d, $J$ = 7.073 Hz, 2H, Ar–H), 7.822–7.837 (d, $J$ = 7.495 Hz, 2H, Ar–H), 7.951–7.993 (d, $J$ = 9.174 Hz, 4H, Ar–H), 8.258–8.266 (t, $J$ = 3.874 Hz, 2H, Ar–H), 8.584–8.601 (d, $J$ = 8.462 Hz, 2H, CH═N), 9.576 (s, OH, enol tautomer), 9.829 (s, 1H, COOH), 15.608/15.787 (s, NH, keto tautomer). $^{13}$C NMR (125 MHz, DMSO-$d_6$, $\delta$ (ppm)): 113.69, 115.56, 118.85, 119.51, 120.48, 124.00, 124.45, 125.87, 126.99, 127.74, 128.41, 128.86, 129.60, 130.50, 132.14, 134.00, 136.10, 136.56, 142.68, 149.86 (Ar–C), 151.02 (Ar = C–N, keto tautomer), 154.33 (CH═N, enol tautomer), 166.96 (COOH), 170.92 (C═O, keto tautomer). Anal. calculated for $C_{29}H_{20}N_2O_4$ (460.48 g mol$^{-1}$): C, 75.64; H, 4.38; N, 6.08. Found: C, 74.14; H, 4.71; N, 6.56. MS (ESI$^+$): $m/z$ calculated for $[M + H]^+$: 461.1501; observed: 461.1489.

**Compound 2b [3,5-bis((*E*)-((2-hydroxynaphthalen-1-yl)methylene)amino)-*N*-(2-hydroxyphenyl)benzamide].** The amido-Schiff base was synthesized according to the published method.[21] Diimine **1b** (1 mmol) was dissolved in a mixture of DCM and EtOH (120 mL, 1 : 2 v/v) under magnetic stirring. A DCM solution (10 mL) of DCC (1 mmol) was added dropwise to a solution of diimine. After stirring the mixture at 0 °C for 30 min, it was treated with 2-hydroxyaniline (1 mmol). The dark yellow mixture was stirred at 0–5 °C for 3 h and room temperature for 24 h. The reaction mixture was left to complete at room temperature for 3 days. The obtained solid was then filtered and dried at room temperature. The product was recrystallized from dichloromethane. Yellow solid; yield: 50%; decomposition point: 311 °C. IR (ATR, $\nu$ (cm$^{-1}$)): 3321 (N–H), 3067 (Ar–H), 2929 (C–H), 2852, 2659 (O–H, naphthol), 2590 (O–H, phenol), 1667/1660 (C═O, amide I), 1622 (C═N), 1606 (C═C), 1558 (amide II), 1483, 1445, 1327 (C–O, phenol), 1308, 1244, 1234 (C–O, naphthol), 1142 (C–N). $^1$H NMR (500 MHz, DMSO-$d_6$, $\delta$ (ppm)): 5.758 (s, 1H, NH), 7.087–7.105 (d, $J$ = 9.116 Hz, 2H, Ar–H), 7.389–7.418 (t, $J$ = 7.320 Hz, 3H, Ar–H), 7.501 (s, 1H, Ar–H), 7.587–7.617 (t, $J$ = 7.422 Hz, 3H, Ar–H), 7.842–7.857 (d, $J$ = 7.829 Hz, 4H, Ar–H), 7.994–8.012 (d, $J$ = 9.106 Hz, 4H, Ar–H), 8.118–8.141 (d, $J$ = 11.342 Hz, 2H, Ar–H), 8.557–8.574 (d, $J$ = 8.419 Hz, 2H, CH═N), 9.776 (s, 1H, OH), 15.533 (s, 2H, NH, keto tautomer). $^{13}$C NMR (125 MHz, DMSO-$d_6$, $\delta$ (ppm)): 112.73, 115.89, 118.30, 119.25, 120.20, 122.23, 124.10, 124.69, 125.95, 127.09, 127.68, 128.05, 128.76, 129.19, 129.72, 130.68, 132.18, 134.21, 135.71, 140.55, 142.84, 146.91 (Ar–C), 150.14 (C–OH), 151.02 (Ar = C–N, keto tautomer), 155.16 (CH═N, enol tautomer), 167.67 (C═O, amide), 170.85 (C═O, keto tautomer). Anal. calculated for $C_{35}H_{25}N_3O_4$ (551.59 g mol$^{-1}$): C, 76.21; H, 4.57; N, 7.62. Found: C, 76.69; H, 4.30; N, 7.73. MS (ESI$^+$): $m/z$ calculated for $[M + H]^+$: 552.1923; observed: 552.1910.

**Compound 3b.** Amido-Schiff base **2b** (0.67 mmol) and Zn(II) nitrate hexahydrate (1.34 mmol) were separately dissolved in EtOH by heating. Then, a colorless solution of the metal cation was added to the reaction flask bearing a yellow solution of **2b**. The mixture was then stirred and refluxed for 3 h. Upon cooling to room temperature, the obtained product was filtered, washed with warm water and EtOH, and dried in air. Yellow solid, yield: 87%, decomposition point: 308 °C. IR (ATR, $\nu$ (cm$^{-1}$)): 3320 (N–H), 3061 (Ar–H), 2928 (C–H), 2852, 2573 (O–H), 1667/1660 (C═O, amide I), 1611 (C═N), 1583/1564 (C═C), 1543 (amide II), 1469, 1442, 1328, 1298 (C–O, naphthol), 1148 (C–N), 641 (Zn–O), 608 (Zn–N). $^1$H NMR (500 MHz, DMSO-$d_6$, $\delta$ (ppm)): 5.759 (s, 1H, NH), 7.087–7.105 (d, $J$ = 9.116 Hz, 2H, Ar–H), 7.389–7.418 (t, $J$ = 7.320 Hz, 3H, Ar–H), 7.501 (s, 1H, Ar–H), 7.587–7.617 (t, $J$ = 7.422 Hz, 3H, Ar–H), 7.842–7.857 (d, $J$ = 7.829 Hz, 4H, Ar–H), 7.994–8.012 (d, $J$ = 9.106 Hz, 4H, Ar–H), 8.118–8.141 (d, $J$ = 11.342 Hz, 2H, Ar–H), 8.513 (s, 2H, CH═N), 9.776 (s, 1H, OH), 11.794 (s, 2H, $H_2O$). Anal. calculated for $[Zn_2(C_{35}H_{23}N_3O_4)_2(H_2O)_4]\cdot 2H_2O$

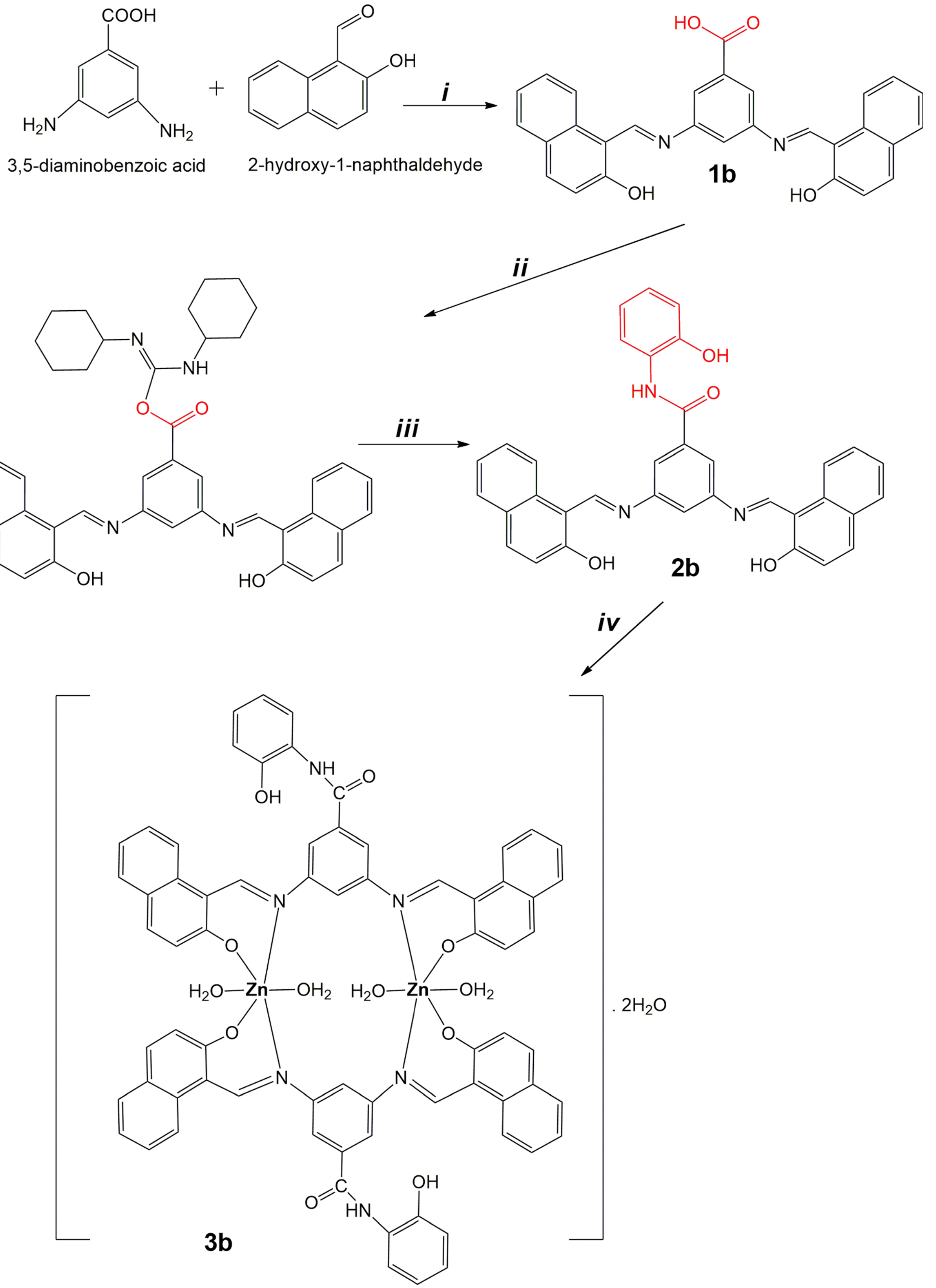

**Scheme 1** The synthesis routes of compounds **1b–3b**: (i) ethanol, reflux (3 h), yield: 84%. (ii) DCC, ethanol, DCM, 0 °C, 30 min. (iii) 2-Hydroxyaniline, 0–5 °C (3 h), at room temperature (24 h), yield: 50%. (iv) $Zn(NO_3)_2 \cdot 6H_2O$, ethanol, reflux (3 h), yield: 87%.

(1338.00 g mol$^{-1}$): C, 62.84; H, 4.37; N, 6.28; Zn, 9.77. Found: C, 63.03; H, 4.37; N, 6.10; Zn, 10.62. MS (ESI$^+$): *m*/*z* calculated for [M]$^+$: 1334.2594; observed: 1334.4074. $\Lambda$ = 1.003 μS ($C$ = 1.0 mM, DMSO) (cell constant = 9.84 cm$^{-1}$, $\Lambda_{\mathrm{DMSO}}$ = 2.87 μS, $\Lambda_{\mathrm{H_2O}}$ = 2.26 μS).

Specific reaction details for these obtained compounds are given in Scheme 1.

### Computational methodology

All molecular calculations were performed using the Gaussian 16 Revision C.02 software. The geometries of all the molecular systems and the property (IR, UV, and NMR) calculations were performed using the Becke three-parameter Lee–Yang–Parr-based (B3LYP) hybrid functional, along with a 6-311++G** (for C, H, N, and O elements) and 3-21G* basis set for Zn to achieve a balance between computational efficiency and accuracy. Harmonic vibrational frequency calculations were performed to confirm that the optimized geometries represented true minima on the potential energy surface (PES). In addition, stability calculations were performed to verify the stability of the wave functions.

### Emission measurements

The emission data were obtained at room temperature using a Hitachi F-4500 fluorescence spectrophotometer equipped with a xenon lamp (150 W). An excitation wavelength ($\lambda_{\mathrm{exc}}$) of 365 nm was used with slit widths of 5 and 10 nm (exc./em.) at 0.5 s response time. For the determination of 'concentration quenched emission,' DMSO and DMF solutions ($C$ = 100 μM and 50 μM) were used and the observations were recorded using fluorimetry. For the investigation of 'aggregation,' DMSO or DMF solution (100 μM) was taken in a quartz cell ($l$ = 1 cm) and increasing volumes (0–4.5 mL) of water were added into the tube by keeping the total volume at 5 mL. The volume ratio of the water in fractions was varied from 0% to 90%. The fluorescence spectra of these fractions were collected 1 day later between 370 nm and 900 nm.

### DPPH radical scavenging assay

The radical scavenging activity of the molecules was measured at room temperature using the DPPH method *via* UV-vis spectroscopy. An appropriate volume of the sample ($C$ = 100 μM, DMSO) was mixed with 1 mL of DPPH solution ($C$ = 200 μM, DMSO), and the total volume was added to 4 mL of pure solvent. The mixtures were then incubated in the dark for 30 min. All measurements were performed in triplicate. The activity was calculated using eqn (1):[22]

$$\%\ \text{DPPH scavenging percentage} = \frac{(A_0 - A_1)}{A_0} \times 100 \qquad (1)$$

where $A_0$ is the absorbance of the positive control (DPPH solution, DMSO) and $A_1$ is the absorbance of the test solution at 517 nm. Ascorbic acid was used as a standard.

## Results and discussion

### Chemistry

The synthesis procedure for these compounds is illustrated in Scheme 1. The formation of diimine-Schiff base **1b** was easily achieved through the direct single condensation of 3,5-diaminobenzoic acid and 2-hydroxy-1-naphthaldehyde in a 1 : 2 mol ratio, owing to its simple and cost-effective preparation. Next, the carboxyl group of **1b** was activated using DCC to generate an intermediate product (3,5-bis((*E*)-((2-hydroxynaphthalen-1-yl)methylene)amino)benzoic(*Z*)-*N*,*N*′-dicyclohexylcarbamimidic anhydride). The treatment of the corresponding acyl lactim with 2-hydroxyaniline led to the amidation of the carboxylic acid and the synthesis of the novel target amido-Schiff base (**2b**). Finally, the zinc complex **3b** was produced from a typical one-pot complexation reaction. The amido-Schiff base (**2b**) has various binding sites and potential N- and O-donor atoms. Therefore, neutral **2b** was reacted with $Zn(NO_3)_2\cdot 6H_2O$ in ethanol at a 1 : 2 molar ratio.

The prepared Schiff bases **1b**–**2b** exist in enol-imine ↔ keto-amine tautomeric equilibrium between the enol and keto forms in the solid state and solution (Scheme S1), which is due to intramolecular O···H···N type hydrogen bonding in the six-membered chelated ring. It is expected that intramolecular proton transfer is shifted towards the keto tautomer for these compounds derived from 2-hydroxy-1-naphthaldehyde. As depicted in Schemes S2 and S3, they also exhibit (*E*)–(*Z*) isomerization around the imine bond. The *Z*-conformer of the enol tautomer and the *E*-conformer of the keto tautomer are less stable species because of having a non-planar structure related to the twist of the naphthyl rings.

These molecules were characterized by FT-IR, $^1$H and $^{13}$C NMR, UV-vis and mass spectroscopies, elemental analysis, thermal analysis, and conductance measurements and supported by density functional theory (DFT) calculations. The C, H, and N analyses of the Schiff bases were in good agreement with the calculated values. The elemental analysis data agreed with the $[Zn_2(C_{35}H_{23}N_3O_4)_2(H_2O)_4]\cdot 2H_2O$ formulation of new dimeric complex **3b.** The charge balance exhibits that **2b** acts as a dianionic ligand to chelate with cations in the complex. For this molecular structure, both centrosymmetrical Zn ions are coordinated by the NO donor set of the two ligands, in which the octahedral coordination environment at each zinc atom is completed by two $H_2O$ molecules. The IR, NMR, and mass spectral data were consistent with the assigned dinuclear structures. Complex formation was established in the solid state and solution from the absorption band positions and resonance signal shifts in the IR and $^1$H NMR spectra, indicating that ligand **2b** bonded with the zinc cation through CH═N and two naphtholate groups. A dinuclear zinc(II) complex was formed at a 2 : 2 (M : L) stoichiometric ratio, which is compatible with some dimeric complex structures in the literature.[23] New complex **3b** is a dimer with a $Zn_2N_2O_6$ core in which the chelating naphtholate oxygen and imine nitrogen atoms from the dianionic tetradentate ligand in the enol form (Scheme S1) and two water molecules. HRMS (ESI$^+$) analysis confirmed the presence of a dimeric dinuclear complex in the gas phase, as evidenced by the characteristic $[M]^+$ signal at $m/z = 1334.4077$. The compounds were stable in air and soluble in DMSO and DMF. The specific conductivity ($\kappa$) of **3b** was calculated as $9.87 \times 10^{-6}$ S cm$^{-1}$ in DMSO ($C = 1.0 \times 10^{-3}$ M) at room temperature. The molar conductivity ($\Lambda_m$) was found to be 9.87 S cm$^2$ mol$^{-1}$, which signifies that it is a non-electrolyte.[24]

### DFT analysis and computational results

No single crystals were obtained for any of the synthesized compounds. Therefore, to support and validate the experimental observations, density functional theory (DFT) calculations were performed for compounds **1b–3b**. All computations were carried out at the B3LYP/6-31+G* level of theory using the Gaussian 16 suite to obtain the lowest-energy geometries.[25] The geometries were optimized in the gas phase and confirmed as true minima using frequency analysis. Additionally, stability calculations were performed to verify the stability of the wave functions.

The optimized ground-state structures are depicted in Fig. 1. The optimized geometries of **1b–3b** clearly indicate the presence of intramolecular N···H–O hydrogen bonding, which supports the experimental conclusion that these compounds exist primarily in the enol tautomeric form in the solid state. These intramolecular H-bonds play a crucial role in stabilizing the molecular conformation and are consistent with the IR spectral signatures and downfield shifts in the NMR spectra. The enol and keto tautomers of **1b** and **2b** were examined to evaluate the stable form. It was obtained that the enol structure has lower energy than the keto form. The enol tautomer is found to be energetically favorable in the gaseous phase, which is the major structure to coordinate with the metal ion. Based on the results, the six-coordinate distorted octahedral geometry is energetically stable for **3b**, where each zinc ion is linked to two coordinated water molecules. Ligand **2b** chelates the metal cation *via* the imine (C=N) nitrogen and hydroxyl oxygen atoms.

Comparisons of the experimental and theoretical IR spectra of the compounds are given in Fig. S1–S3. The DFT-calculated IR spectra (keto-tautomer) reproduced the key vibrational bands of the experimental spectra. Specifically, the imine $\nu$(C=N) stretching vibrations were observed at ~1620–1611 cm$^{-1}$, closely matching the experimental values (1620 cm$^{-1}$ for **1b**, 1622 cm$^{-1}$ for **2b** and 1611 cm$^{-1}$ for **3b**). Similarly, the calculated $\nu$(C–H) and $\nu$(O–H) stretching frequencies were in agreement with the IR results, confirming the tautomeric form and coordination environment.

The computed chemical shifts for $^1$H (Fig. S4–S6) and $^{13}$C NMR (Fig. S7–S9) align well with the experimental spectra, further validating the proposed structures of the keto-tautomer. For **1b–2b**, the signal at ~15.8 and 15.6 ppm is attributed to the naphtholic NH protons of the keto tautomer. A broad peak within the range of 6.0–9.0 ppm was assigned to the enamine (=CH–N) and aromatic protons. The signal at 4.6 ppm corresponded to the NH proton of the amide moieties. For **3b**, the imine and aromatic ring protons are observed at ~6.0–10.0 ppm. In the $^{13}$C NMR spectra, the peaks at ~172 ppm and ~154 ppm correspond to (C=O) and (C=N) carbon atoms of the enol and keto tautomers for **1b–2b**. Two different signals were at ~177 and ~180 ppm belonging to naphtholic (C–O) carbons in the zinc complex. The theoretical downfield shifts observed for the imine protons support their involvement in the tautomerism and coordination with Zn(II). The calculated data confirmed that **1b** and **2b** existed in equilibrium between the enol and keto forms, with the keto form stabilized in polar media, as reflected in both the experiment and computation.

TD-DFT calculations provided UV-vis absorption spectra in the gas phase for the keto-tautomer (Fig. S10–S12), which closely matched the experimental $\lambda_{max}$ values. The simulated absorption bands at 432 nm (**1b**) and 427 nm (**2b**) were in excellent agreement with the experimental results, supporting the assignments for intraligand $\pi \rightarrow \pi^*$ and $n \rightarrow \pi^*$ transitions for the keto tautomer. The spectrum of the zinc complex exhibits an absorption maximum at 396 nm. The observed spectral change confirmed that this band was shifted to a higher energy region upon complexation.

The calculated optical gaps due to the highest occupied molecular orbital (HOMO) and lowest unoccupied molecular orbital (LUMO) also corroborate the experimentally derived optical band gaps from the Tauc and ASF methods. The DFT-derived gaps were 3.188 eV (**1b**), 3.202 eV (**2b**), and 3.054 eV (**3b**) (Fig. 2 and Fig. S13), which closely aligned with the experimental direct band gap values of ~4.34–4.46 eV. These DFT-calculated gaps are lower than the corresponding experimentally estimated optical bandgaps, which is expected, as DFT, particularly with hybrid functionals such as B3LYP, is well known to underestimate bandgap energies due to the inherent approximations in the exchange–correlation functionals.

The HOMO of the ligands is mainly localized on the aromatic $\pi$-system and phenolic oxygen, while the LUMO resides on the imine $\pi^*$ orbital and adjacent aromatic rings. Upon complexation in **3b**, the HOMO–LUMO distribution shifts to include the Zn coordination sphere, indicating enhanced conjugation and intramolecular charge transfer (ICT) characteristics. Nonetheless, the computational trend in gap energies correctly mirrors the experimental results, validating the electronic structure and photophysical behavior.

### Spectral analysis

**IR spectra.** In the infrared spectrum of **1b** (Fig. S1), the broad absorption band centered at 2763 cm$^{-1}$ is attributed to the COOH frequency. The weak band at 2502 cm$^{-1}$ is related to the naphtholic $\nu$(O–H) stretching vibration. The $\nu$(C=O) frequency of the carboxyl group was 1702 cm$^{-1}$. The imine $\nu$(C=N) and $\nu$(C–H) vibrations were observed at 1620 and 2870 cm$^{-1}$ for **1b**, existing mainly in the enol tautomer with N···H–O interactions in the solid state. The $\nu$(C–H) and $\nu$(C=C) frequencies of the aromatic ring appeared at 3053 cm$^{-1}$, 1587, and 1527 cm$^{-1}$. The band at 1301 cm$^{-1}$ is attributed to the carboxylic $\nu$(C–O) frequency. The naphtholic $\nu$(C–O) frequency was observed at 1203 cm$^{-1}$, indicating the existence of an enol tautomer. For **2b** (Fig. S2), the $\nu$(O–H) carboxyl band disappeared, as expected.

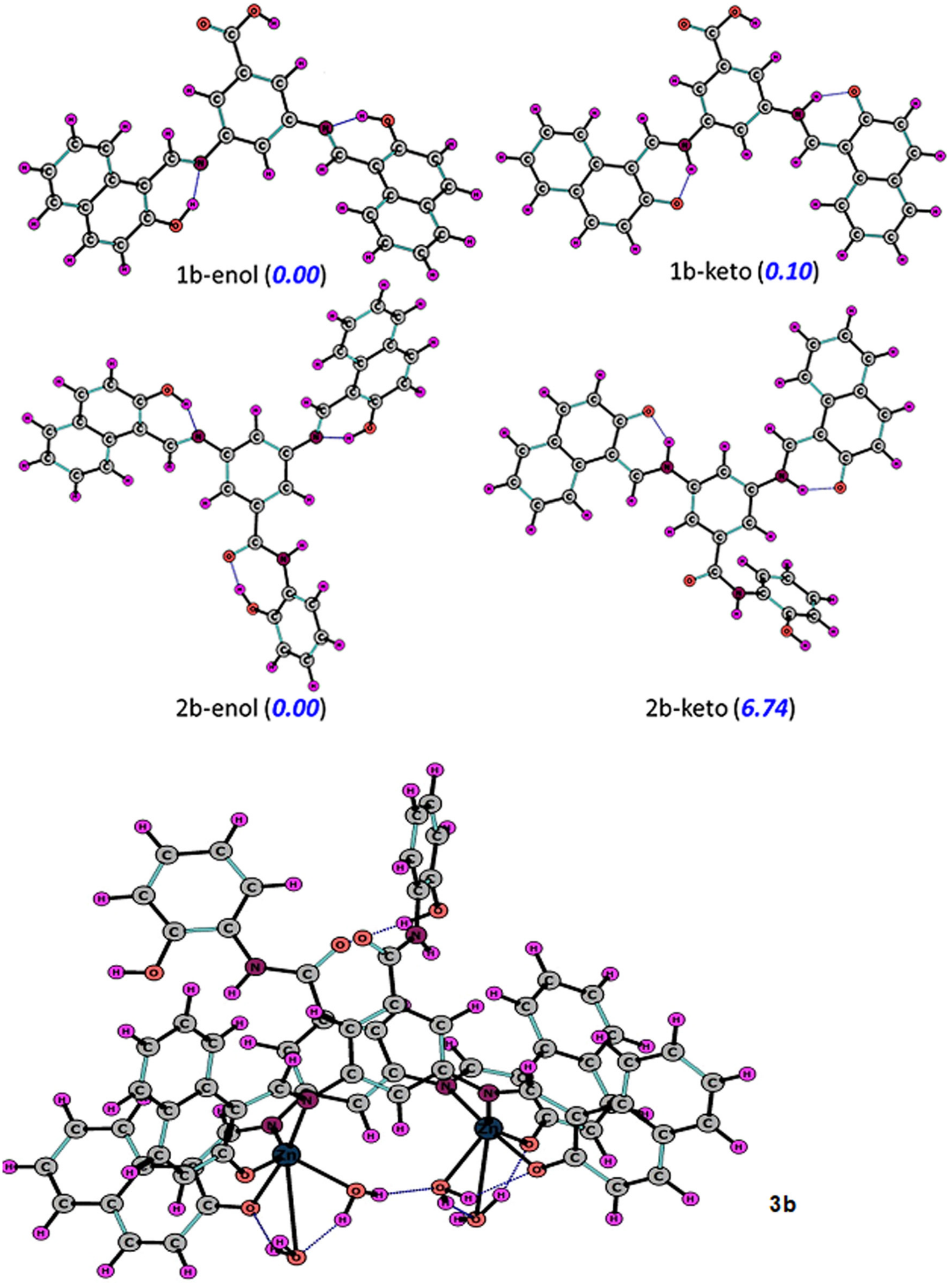

Fig. 1 Optimized geometries of molecules **1b–3b**, with relative energies in parentheses (kcal mol$^{-1}$).

The naphtholic $\nu$(O–H) stretching vibration frequency is observed at 2659 cm$^{-1}$. The $\nu$(N–H) and $\nu$(C=O) frequencies of the amide A and I bands appear at 3321 and 1667/1660 cm$^{-1}$,[26] indicating the formation of the proposed skeleton structure. The amide II band, due to the combination of $\nu$(C–N) stretching and $\delta$(N–H) bending vibrations, was observed at 1558 cm$^{-1}$. The $\nu$(O–H) frequency in the weak intramolecular hydrogen bonds (O–H···NH) due to the new phenyl ring was observed at 2590 cm$^{-1}$. The imine $\nu$(C=N) and (C–H) bands were centered at 1622 and 2929 cm$^{-1}$, confirming that **2b** forms

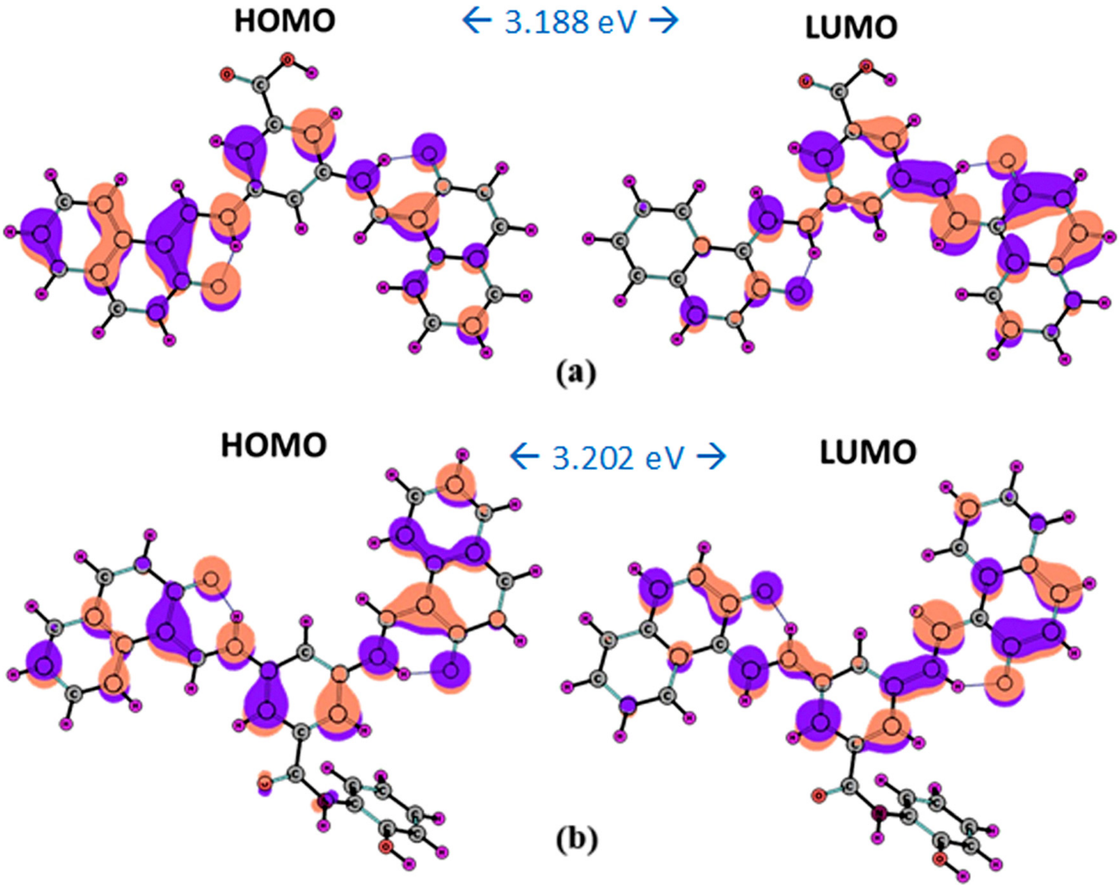

Fig. 2 Frontier MOs of (a) **1b** and (b) **2b** (keto tautomer).

the enol tautomer. The aromatic ring $\nu$(C–H) and $\nu$(C=C) bands peaked at 3067 $cm^{-1}$ and 1606 $cm^{-1}$. $\nu$(C–O) frequencies were observed at 1327 $cm^{-1}$ and 1234 $cm^{-1}$. For **3b** (Fig. S3), the amide $\nu$(N–H) frequency appeared at 3320 $cm^{-1}$. There were no appreciable changes in the bands corresponding to amide I and II vibrations. These bands were observed at 1667/1660 $cm^{-1}$ and 1543 $cm^{-1}$, indicating that the amide carbonyl functional group was not bound to metal ions. The $\nu$(O–H) frequency of the phenol group appeared at 2573 $cm^{-1}$. Upon complex formation, the naphtholic (O–H) band was absent, and the $\nu$(C–O) frequency shifted to 1298 $cm^{-1}$ compared to that of the free ligand **2b**, supporting the deprotonation of the hydroxyl groups. The $\nu$(C=N) frequency was shifted to 1611 $cm^{-1}$. A significant negative shift (11 $cm^{-1}$) in this stretching mode indicated that the imine nitrogen atom was coordinated to zinc. The aromatic $\nu$(C–H) and $\nu$(C=C) vibrations peaked at 3061 $cm^{-1}$ and 1583/1564 $cm^{-1}$. The new absorption bands at 641 $cm^{-1}$ and 608 $cm^{-1}$ were assigned to $\nu$(Zn–O) and $\nu$(Zn–N), respectively.

**NMR spectra.** $^1$H NMR data of the compounds were recorded in DMSO-$d_6$. For **1b** (Fig. S14), the chemical shift of the carboxyl OH proton was observed at $\delta_H$ 9.829 ppm as a singlet. The singlet signals at $\delta_H$ 15.608 and 15.787 ppm were assignable to the naphtholic NH protons, which confirms the existence of the keto tautomer as a significant contributor in the equilibrium. A low-integral singlet at $\delta_H$ 9.576 ppm and a doublet in the range of $\delta_H$ 8.584–8.601 ppm were attributed to the signals of the OH and imine protons of the enol structure, respectively. The $^3J_{(NH,CH)}$ coupling constant of the imine signal was recorded as 8.462 Hz, suggesting a proton transfer from the hydroxyl group to the imine-N atom. Aromatic protons were observed between $\delta_H$ 7.071 ppm and 8.266 ppm. According to these spectral results, **1b** exists as a mixture of enol and keto forms in the solution. In **2b** (Fig. 3a), the carboxyl–OH signal disappeared. The signal of the naphtholic NH protons was observed at $\delta_H$ 15.533 ppm, which gave an upfield shift with respect to that of the corresponding signal of the diimine. In addition, the imine protons shifted slightly downfield compared with that of **1b** and were observed in the range of $\delta_H$ 8.557–8.574 ppm as a doublet. The obtained results confirmed the shift in the intramolecular proton transfer equilibrium from the enol tautomer to the keto form in DMSO. Phenol OH and amide NH protons appeared at $\delta_H$ 9.776,[27] and 5.758 ppm, respectively. The aromatic protons were signaled within the range of $\delta_H$ 7.087–8.141 ppm. In the $^1$H NMR spectrum of **3b** (Fig. 3b), the naphtholic NH protons of the free ligand **2b** were absent. The singlet signal at $\delta_H$ 11.794 ppm was assigned to coordinated $H_2O$ molecules. The signal due to the azomethine protons underwent an upfield shift to $\delta_H$ 8.513 ppm. This may demonstrate the coordination nature of **2b** *via* imino

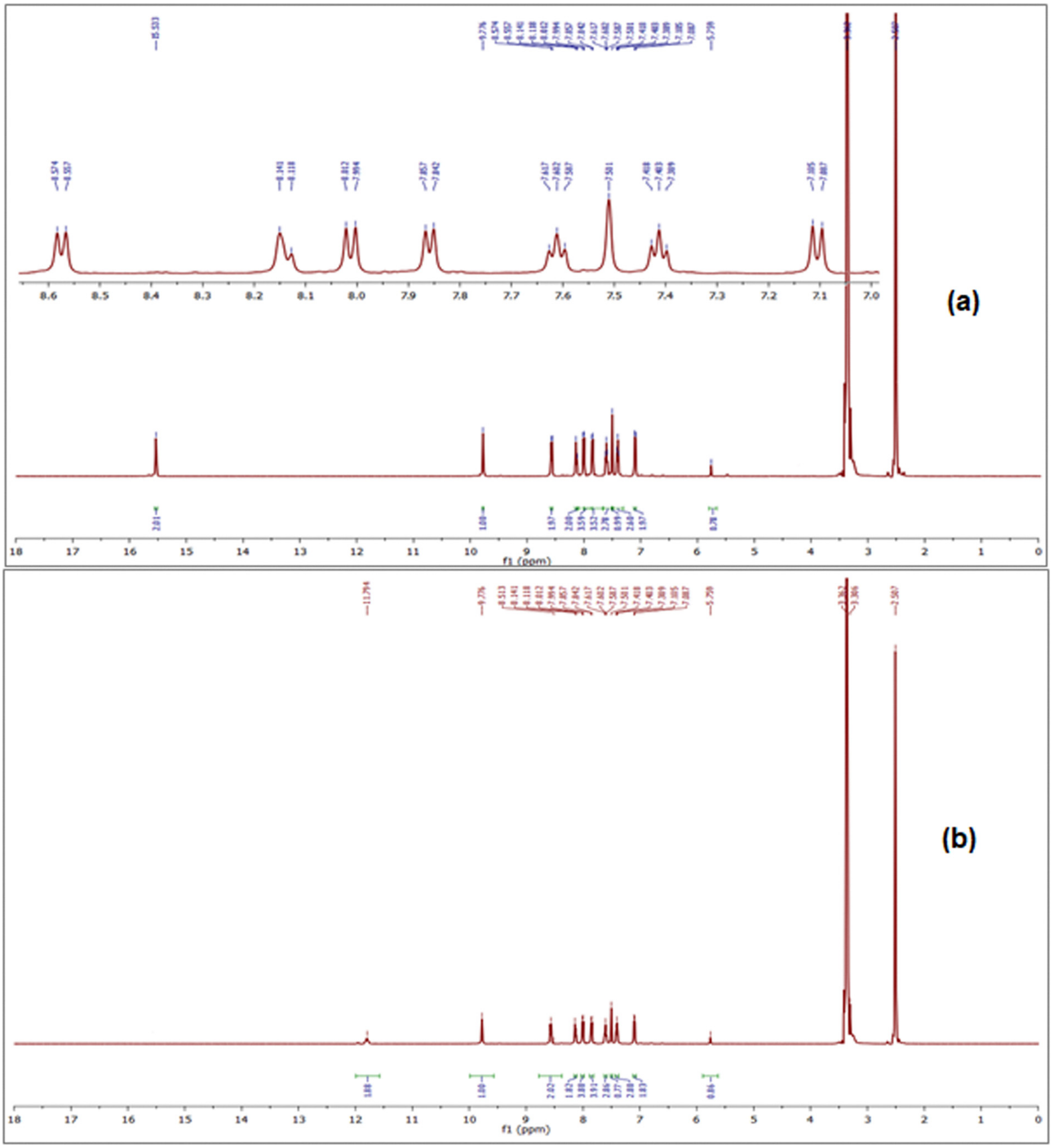

Fig. 3 $^1$H-NMR spectra of (a) **2b** and (b) **3b** in DMSO-d$_6$.

N-atoms and deprotonated hydroxyl O-atoms upon binding with metal ions. Phenolic OH and amidic NH protons were observed at $\delta_H$ 9.776 and 5.759 ppm, respectively, in the complex structure, indicating that these groups did not participate in complexation. **3b** exhibited approximately the same peaks for aromatic protons, similar to those of **2b**.

The proton-decoupled $^{13}$C NMR spectrum of **1b** displayed 24 peaks in DMSO-d$_6$ (Fig. S15). The signal at $\delta_C$ 166.96 ppm belonged to the carboxyl carbon. The signal at $\delta_C$ 170.92 ppm was attributed to the carbonyl carbon of the keto tautomer. The peaks at $\delta_C$ 154.33 and 151.02 ppm may be assigned to the (C═N) and (═C–N) carbons of the enol and keto tautomers, respectively. Other aromatic carbons appeared between $\delta_C$ 113.69 ppm and 149.86 ppm. The $^{13}$C NMR spectrum of **2b** showed 27 peaks (Fig. S16). The carboxyl carbon peak was absent with the observation of a new peak at $\delta_C$ 167.67 ppm due to the carbonyl carbon atom of the amide band. The other carbonyl carbon assigned to the keto tautomer was seen at $\delta_C$ 170.85 ppm. The imine and the enamine carbons were detected at $\delta_C$ 155.16 and 151.02 ppm. The peak at $\delta_C$ 150.14 ppm may be due to the phenolic carbon of new benzene ring. Aromatic carbons resonated in the range of $\delta_C$ 112.73 and 146.91 ppm.

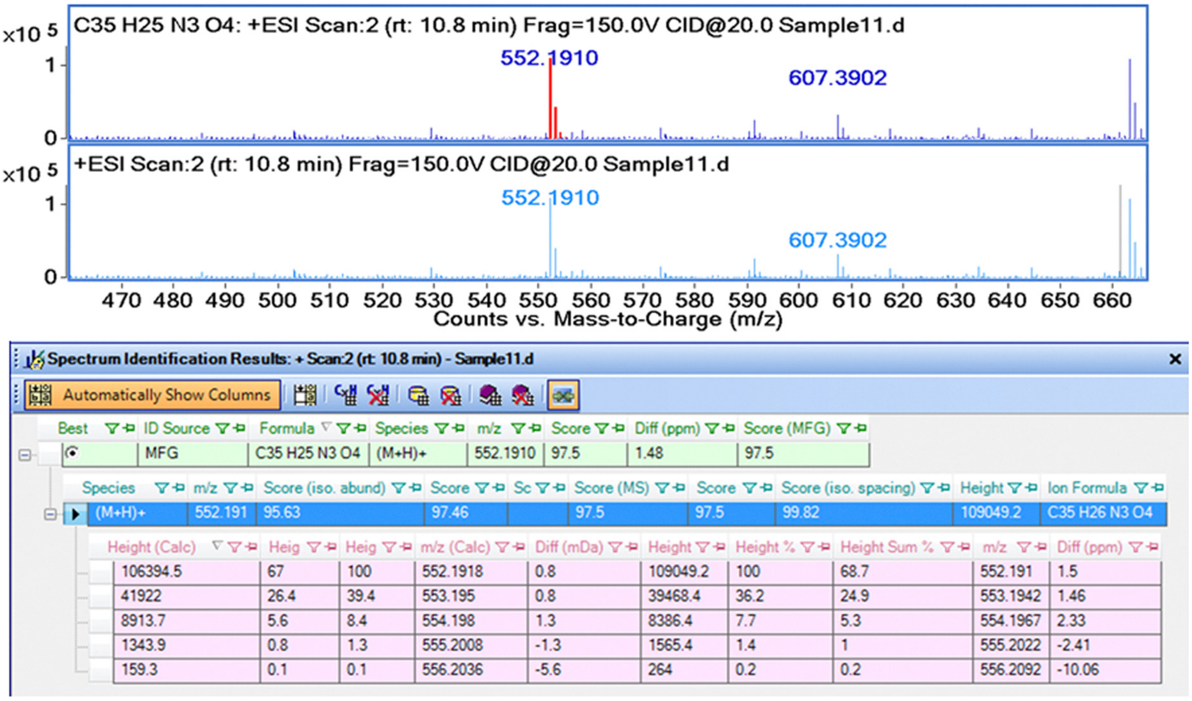

| Best | ID Source | Formula | Species | m/z | Score | Diff (ppm) | Score (MFG) |
|---|---|---|---|---|---|---|---|
| ● | MFG | C35 H25 N3 O4 | (M+H)+ | 552.1910 | 97.5 | 1.48 | 97.5 |

| Species | m/z | Score (iso. abund) | Score | Sc | Score (MS) | Score | Score (iso. spacing) | Height | Ion Formula |
|---|---|---|---|---|---|---|---|---|---|
| (M+H)+ | 552.191 | 95.63 | 97.46 | | 97.5 | 97.5 | 99.82 | 109049.2 | C35 H26 N3 O4 |

| Height (Calc) | Heig | Heig | m/z (Calc) | Diff (mDa) | Height | Height % | Height Sum % | m/z | Diff (ppm) |
|---|---|---|---|---|---|---|---|---|---|
| 106394.5 | 67 | 100 | 552.1918 | 0.8 | 109049.2 | 100 | 68.7 | 552.191 | 1.5 |
| 41922 | 26.4 | 39.4 | 553.195 | 0.8 | 39468.4 | 36.2 | 24.9 | 553.1942 | 1.46 |
| 8913.7 | 5.6 | 8.4 | 554.198 | 1.3 | 8386.4 | 7.7 | 5.3 | 554.1967 | 2.33 |
| 1343.9 | 0.8 | 1.3 | 555.2008 | -1.3 | 1565.4 | 1.4 | 1 | 555.2022 | -2.41 |
| 159.3 | 0.1 | 0.1 | 556.2036 | -5.6 | 264 | 0.2 | 0.2 | 556.2092 | -10.06 |

Fig. 4 TOF-MS spectrum of **2b**.

The $^{13}$C NMR spectrum of **3b** could not been obtained because of its solubility problem in deuterated-DMSO.

**Mass spectra.** Q-TOF mass spectral patterns of the newly synthesized compounds confirmed the proposed empirical formula. The detected molecular masses, fragment ions, and retention times (RT) are listed in Table S1. Diimine **1b** exhibited abundant molecular ions $[(C_{29}H_{20}N_2O_4) + H]^+$ at $m/z$ = 461.1489 with an 8.2 a retention time. The peak at $m/z$ 921.2901 is consistent with the theoretical mass value of the dicarboxylic acid dimer structure of diimine, which is related to the formation of intermolecular H-bonds between carboxylic OH groups. An important fragment was observed at $m/z$ 214.0861, which may be related to the loss of the $(C_{11}H_8O)$, $(C_4H_4)$, and (COOH) components of the diimine structure (Fig. S17). The mass spectrum of **2b** showed a molecular ion $[(C_{35}H_{25}N_3O_4) + H]^+$ at $m/z$ = 552.1910 as a base peak within a 10.8 min retention time (Fig. 4). The *m*-phenylenediamine-based Schiff bases can create mononuclear, homo- and hetero-dinuclear complexes in ligand : metal ratios of 1 : 1, 2 : 1, 1 : 2, and 2 : 2, or oligonuclear metal complexes because they behave as bridges that link metal ions.[28,29]

The correlations of counts *vs.* acquisition time (min) and mass-to-charge ($m/z$) for **3b** are given in Fig. 5. The presence of dimer species 2 : 2 $[M_2L_2]$ of complex **3b** was confirmed through mass spectrometry. The component ion at $m/z$ = 1334.4077 was consistent with symmetrical dinuclear/dimeric complex formation, which shows the stability of the dimeric ion in the gas phase. The ions' stability in the gas phase depends on the intensity of the $m/z$ signals, which is responsible for relative ion abundance. In the mass spectrum, the most abundant peak was found to be a monomeric $[ML]^+$ species. The amount of the fragments due to the dimeric (1334.4077 $m/z$) and monomeric (667.7077 $m/z$) structures of **3b** is ∼50% and 100% abundance. The coordinated water molecules stabilize dimeric structures due to the formation of strong intra- and intermolecular hydrogen bonds. But aromatic rings are not close to planar in complex **3b**, while the naphthalene rings show a nearly planar conformation in the free ligand. Decreased planarity of the conjugated π-system and the presence of steric hindrance of the *N*-(2-hydroxyphenyl)formamide group may lead to a decrease in the stability of the dimeric structure at L : M ratio 2 : 2. Therefore, the equilibria $[M_2L_2] \leftrightarrow 2[ML]$ are shifted to the right to increase the percentage of the monomeric species. The other fragment at $m/z$ 214.2086 was attributable to the following molecule 2-(((3-aminophenyl)amino)methyl)phenol (chemical formula $C_{13}H_{14}N_2O$).

## TGA-DTA thermograms

Thermograms of zinc complex **3b** are given in Fig. 6. All thermoanalytical results are summarized in Table 1. The TGA curve displayed a first decomposition reaction in the temperature range of 28 °C and 255 °C under a nitrogen atmosphere, where the average mass loss is 19.71%. This loss may belong to elimination of coordinated and uncoordinated $H_2O$ molecules and a $(C_{11}H_7O)$ group. In the 2nd step, the mass loss was 45.70% over 255–464 °C. The 3rd decomposition reaction was observed between temperatures of 464 °C and 764 °C with a slow decrease in the mass (21.37%). The obtained total mass loss (86.78%) was due to degradation of organic ligand molecules, where the residue may be assumed as a mixture of zinc oxide and zinc hydroxide in the remaining part. The DTA curve of **3b** showed that the endothermic peaks at 247, 316 and

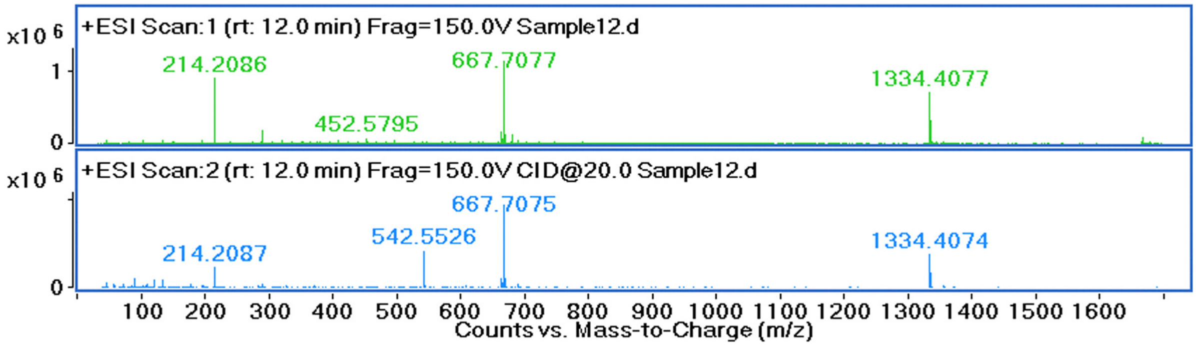

Fig. 5 TOF-MS spectrum of **3b**.

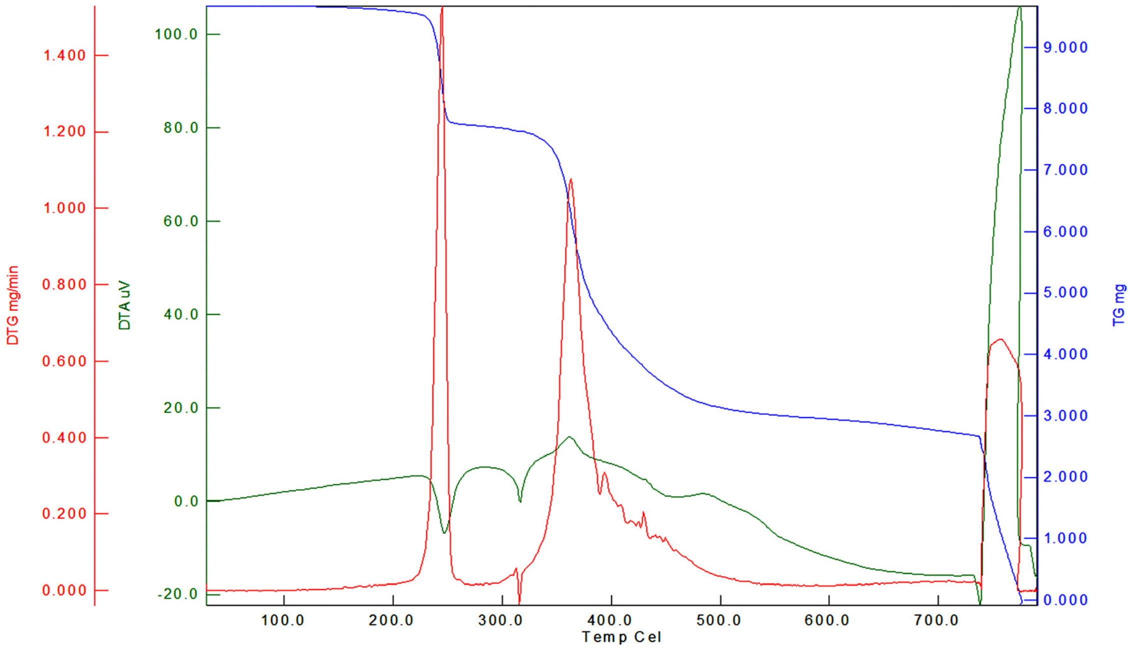

Fig. 6 TGA-DTA thermograms of **3b**.

Table 1 Thermal decomposition of dimeric Zn(II) complex **3b**

| Step | Δ*T* (°C) | $DTA_{max}$ (°C) | $DTG_{max}$ (°C) | DTG (μg $min^{-1}$) | Mass loss (%) |  | Assignment | Residue (%) |  |
|---|---|---|---|---|---|---|---|---|---|
|  |  |  |  |  | Found | Calc. |  | Found | Calc. |
| 1 | 28.78–254.91 | 247.03 (*endo*) | 244.56 | 1538.203 | 19.71 | 19.67 | Loss of 6 mol $H_2O$<br>1 mol ($C_{11}H_7O$) |  |  |
| 2 | 254.91–463.97 | 316.17 (*endo*)<br>361.58 (exo)<br>463.88 (*endo*) | 362.69 | 1078.125 | 45.70 | 44.92 | Loss of 1 mol ($C_{35}H_{23}N_3O_3$)<br>1 mol ($C_4H_4O$) | 1 mol ZnO<br>1 mol $Zn(OH)_2$<br>13.22 13.51 |  |
| 3 | 463.97–764.24 | 757.68 (*exo*) | 757.76 | 658.734 | 21.37 | 21.89 | Loss of 1 mol ($C_{20}H_{10}N_3$) |  |  |

463 °C overlapped with the decomposition reactions in the 1st and 2nd step in the TGA thermogram. The exothermic peak was observed at 361 °C, which is related to other mass loss in the TGA curve. An exothermic peak was seen at 755 °C under an open air $O_2$ atmosphere.

## Optical properties

**Electronic absorption of the compounds.** Enol–keto tautomerism is affected by either the solvent nature or light. Polar solvents stabilize the keto-amine form in the ground state, which can be explained by the more polar electronic structure of this tautomer.[30] The existence of the NH form is manifested by absorption above 400 nm.[31] The absorption spectra of the synthesized compounds were measured at room temperature in DMSO and DMF at various concentrations. As listed in Table S2, it was noted that the spectra showed nearly no difference between these solutions. In DMSO ($C = 100\ \mu$M), diimine **1b** has a maximum at 320 nm, a shoulder at 391 nm, and a dual absorption band at 444 and 467 nm, while four maxima were observed at 322, 394, 443, and 468 nm for **2b** (Fig. S18). In DMF ($C = 100\ \mu$M), **1b** exhibited intense absorption at 320 nm and 390 nm and dual absorption at 442 and 465 nm (Fig. S19). In the presence of **2b**, bands appeared at 320 nm, 393 nm, 440 nm, and 465 nm. The highest energy absorption peaks were ascribed to $\pi \rightarrow \pi^*$ and $n \rightarrow \pi^*$ transitions of the (C═N) bond of the azomethine group, respectively, in which the band at 320–322 nm is characteristic of the enol form. The lowest energy dual maxima were assigned to $n \rightarrow \pi^*$ transitions of the (C═O) bond of the carbonyl group. The results showed that both **1b** and **2b** may be mixtures of enol and keto tautomers at room temperature. The keto form was favored in polar aprotic DMSO and DMF solutions, which was in accordance with the NMR results. These molecules lie on a two-fold rotation around the imine C═N bond axis,[32] which are in the *trans*(*E*) and *cis*(*Z*) configuration for the enol–keto tautomers of **1b** and **2b**, respectively (Schemes S2 and S3).

Diamagnetic Zn(II) ions with a d$^{10}$ configuration can exhibit various coordination numbers and geometries. The polarizing power, size, and steric requirements of the ligand molecules influence the stereochemistry of the zinc complexes. At a concentration of 100 μM, complex **3b** contained absorption bands at 321, 395, 444, and 468 nm in DMSO and 322, 391, 439, and 465 nm in DMF. The absorption bands of ligand **2b** were not significantly affected by chelation, but the $\lambda_{\max}$ values due to the imino bond showed strong intensity bands, confirming the coordination with metal ions. The complex geometry d–d transition bands were not observed in the UV-vis spectrum. Accordingly, an octahedral geometry may be suggested for the coordination sphere around the Zn(II) ion in **3b** on the basis of the spectral results in the literature.[33–35] When the concentration was lower than 100 μM, the absorption of **1b–3b** complied with Beer's law, indicating a lack of aggregation.

The chemical stability of the compounds was evaluated over time. UV-vis spectra were recorded a few months later (Fig. S20). In the case of **1b**, two absorption maxima were observed at 320 and 355 nm in DMSO at 100 and 50 μM, respectively. The observation of a broad tail instead of a dual band above 400 nm may be attributed to the presence of intermolecular H-bonds with polar protic solvent molecules. Absorption bands appeared at 320, 353, 443, and 468 nm, and 320, 354, 442, and 467 nm for **2b** and **3b**, respectively. The absence of any new peaks confirmed that **1b–3b** were stable in the solution over time. Intramolecular interactions may play a decisive role in stabilization. The stability of the molecules was studied using the quantum chemical parameters of the molecular orbital structures.

**Optical band gap energy.** The optical bandgap of photonic materials is an important parameter for their potential use in optoelectronic applications. The band gap energy ($E_g$) between the valence and conduction bands was determined using the UV-vis absorption spectrum. The Tauc method describes the optical bandgap as a function of the absorption coefficient ($\alpha$) and incident photon energy ($h\nu$). The absorption coefficient is defined by eqn (2),[36] where $l$ is the thickness of the quartz cuvette (10 mm).

$$\alpha = 2.303 \times \frac{\text{Absorbance}}{l} \tag{2}$$

The $E_g$ (eV) value is the cut-off point at the energy axis ($\alpha h\nu = 0$) of the straight line of the Tauc plot in eqn (3).[37] Here, $A$ is an energy-independent constant (1 for an ideal situation). The $n''$ constant depending on the electron transition processes can take 1/2, 2, 3/2, and 3 values for the calculation of the allowed direct and indirect, forbidden-direct, and indirect transitions, respectively.

$$(\alpha h\nu) = A(h\nu - E_g)^n \tag{3}$$

The absorbance fitting method (ASF) describes the optical band wavelength ($\lambda_g$), which is the cut-off point at the $\lambda^{-1}$ axis of the straight part of eqn (4).[38] $\lambda_g$ was determined by extrapolating the curve of $(A\lambda^{-1})^{1/n}$ as a function of $(\lambda^{-1})$. Here, $B_1$ and $B_2$ are constants and $A(\lambda)$ is the absorbance at $\lambda$. $E_g$ (eV) was calculated using eqn (5):[39]

$$A(\lambda) = B_1 \lambda \left[\frac{1}{\lambda} - \frac{1}{\lambda_g}\right]^n + B_2 \tag{4}$$

$$E_g = \frac{1240}{\lambda_g} \tag{5}$$

The aligned direct ($E_d$) and indirect ($E_i$) transition band gaps of the newly synthesized compounds obtained by the Tauc and ASF methods are shown graphically in Fig. 7 and Fig. S21–S23. At a 100 μM concentration, the $E_d$ gap energy of **1b–3b** was calculated between 4.34 and 4.46 eV in DMSO, while it was found to be in the range of 4.41–4.49 eV in DMF. At a concentration of 50 μM, the $E_d$ energy value was within the range of 4.36–4.46 eV in these solutions. In DMSO, the $E_i$ energy of the compounds was found to be between 4.03–4.18 eV and 4.06–4.25 eV at 100 μM and 50 μM concentrations. The $E_i$ value was determined between 4.23–4.33 eV and 4.09–4.30 eV in DMF.

Metal ions can decrease the energy gap of the HOMO level and $\pi \rightarrow \pi^*$ molecular orbitals of the ligand, because of increasing conformational rigidity in the structure. Despite this, new zinc complex **3b** displayed similar $E_d$ and $E_i$ values as the corresponding ligand **2b**. It was noticed that all compounds have optical band gaps of $\sim$4 eV, which may be due to their semiconductor behavior.[40] On the other hand, the obtained results of the Tauc and ASF methods were found to be very close to each other. As listed in Table 2, the $E_d$ energies were generally determined to be higher than the $E_i$.

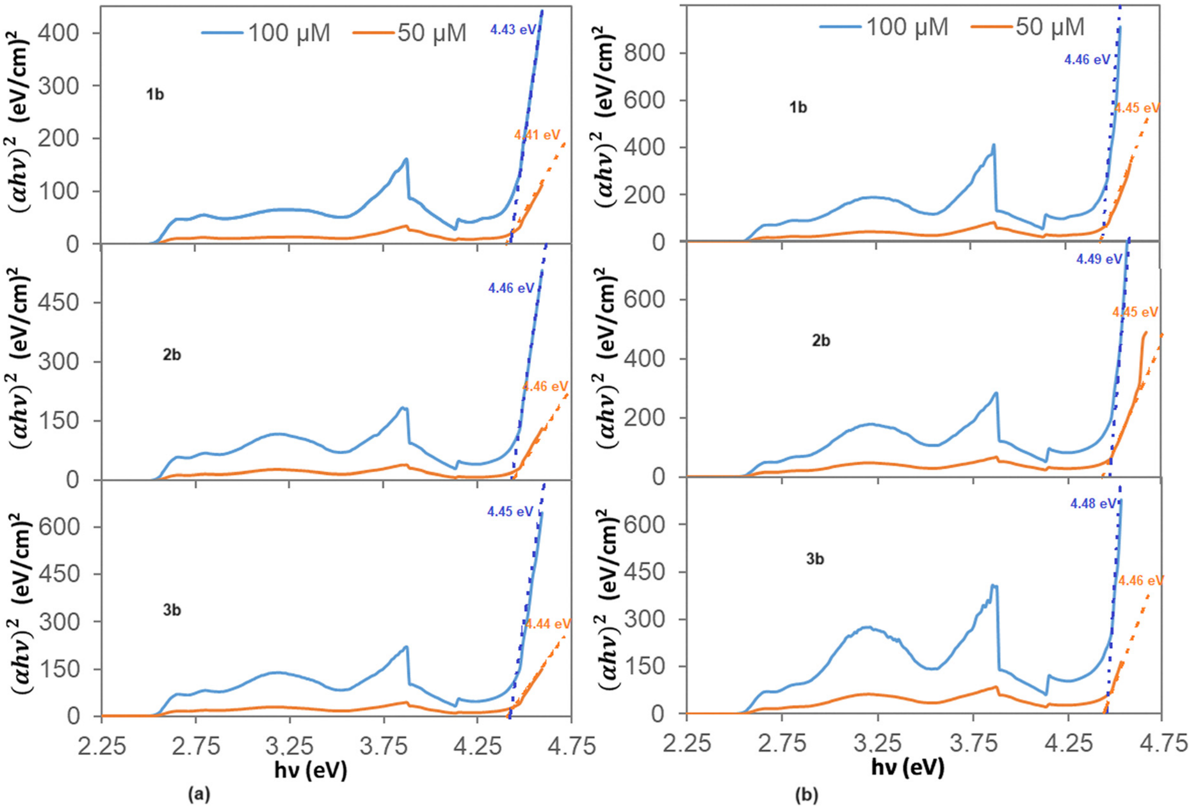

Fig. 7 Tauc's plots for the direct allowed transition of **1b–3b** in (a) DMSO and (b) DMF.

Table 2 The optical band gap energies of **1b**–**3b**

| Media | **1b** Tauc method<br>$E_d$ (eV)<br>$E_i$ (eV) | **1b** ASF method<br>$E_d$ (eV)<br>$E_i$ (eV) | **2b** Tauc method<br>$E_d$ (eV)<br>$E_i$ (eV) | **2b** ASF method<br>$E_d$ (eV)<br>$E_i$ (eV) | **3b** Tauc method<br>$E_d$ (eV)<br>$E_i$ (eV) | **3b** ASF method<br>$E_d$ (eV)<br>$E_i$ (eV) |
|---|---|---|---|---|---|---|
| DMSO (100 μM) | 4.43<br>4.10 | 4.34<br>4.03 | 4.46<br>4.16 | 4.39<br>4.09 | 4.45<br>4.18 | 4.44<br>4.07 |
| DMSO (50 μM) | 4.41<br>4.10 | 4.36<br>4.08 | 4.46<br>4.25 | 4.43<br>4.14 | 4.44<br>4.20 | 4.38<br>4.06 |
| DMF (100 μM) | 4.46<br>4.32 | 4.44<br>4.23 | 4.49<br>4.28 | 4.44<br>4.28 | 4.48<br>4.32 | 4.41<br>4.33 |
| DMF (50 μM) | 4.45<br>4.23 | 4.41<br>4.09 | 4.45<br>4.21 | 4.41<br>4.14 | 4.46<br>4.30 | 4.38<br>4.24 |

**Emission of the compounds.** Solvent polarity affects the fluorescent behavior of fluorophores belonging to the nature of the formation of intramolecular charge (ICT) and photo-induced electron (PET) transfers in such molecules or the occurrence of intermolecular solute–solvent interactions and charge transfer complex.[41] Intramolecular proton transfer reaction in the excited state (ESIPT) can favour and stabilize the keto form for most of the naphthalidene-aniline ligands,[42] which is only the light-emissive tautomer in nonpolar solvents.[43] The excited state of the fluorescent *Z*-keto tautomer returns back to the ground state by a thermal process or displaying emission or undergoing geometric *cis–trans* isomerization. Upon chelating with metal ions, the hydroxyl protons of the ligands are deprotonated and the ESIPT phenomenon is hindered. Coplanarity and conformational rigidity of the molecular structure increase as a result of the complexation-induced inhibition of rotation around the C═N functional group. This hampers the non-radiative decay route, such as degradation and vibrational relaxation,[44] and so fluorescence enhancement can be observed through the combination of chelation-enhanced fluorescence (CHEF), the complexation-induced internal charge transfer (ICT) or PET mechanisms.[45]

The fluorescence behavior of Schiff bases **1b**–**2b** is strongly influenced by π-conjugation, conformational rigidity, and intermolecular interactions. The *E*/*Z* photoisomerization arising from free rotation around the imine bond, together with the flexibility of the naphthyl rings, may facilitate non-radiative relaxation pathways, resulting in relatively weak fluorescence that is consistent with ACQ-type behavior in the aggregated state. In contrast, the restriction of intramolecular rotational and vibrational motions (RIM) suppresses non-radiative decay and promotes radiative transitions, leading to enhanced fluorescence characteristics of AIE-type behavior. Metal ion coordination provides an additional strategy to modulate the photophysical properties of the hybrid Schiff base **2b**. $Zn^{2+}$ chelation disrupts the intramolecular O–H···N hydrogen bonds, thereby suppressing the ESIPT process to favor the enol tautomer of the imine moiety. Coordination of $Zn^{2+}$ *via* the imine nitrogen and hydroxyl oxygen rigidifies the molecular framework, producing chelation-enhanced fluorescence (CHEF). This restricts intramolecular rotations and inhibits photoinduced electron transfer (PET), which often quenches the fluorescence in free ligands. The diamagnetic $d^{10}$ configuration of $Zn^{2+}$ can modify both the electronic structure and molecular dynamics of the fluorophore. In particular, processes such as intramolecular charge transfer (ICT) and metal–ligand charge transfer (MLCT) may become more prominent. These electronic effects can minimize non-radiative decay pathways, thereby suppressing ACQ and activating AIE-related emission pathways.

The fluorescence spectra of the newly synthesized compounds are shown in Fig. 8 and 9, respectively. All compounds were yellow in color in DMSO and DMF solutions. Once excited with a xenon lamp ($\lambda_{exc}$ = 365 nm), the compounds emitted green or bluish-green/greenish-blue fluorescence at room temperature. This emission appeared visibly brighter in the DMSO solution. For diimine-Schiff base **1b**, the emission maxima were located at 426 and 504 nm, originating from intraligand charge-transfer (ILCT) transitions. This highest-energy emission was attributed to the high π* level of the former. In the case of amido-Schiff base **2b**, the emission band at 426 nm underwent a 33 nm red shift with respect to that of **1b** (Table S2). The maximum emission was also observed at 504 nm in DMSO ($C$ = 100 μM), which may have been caused by enol–keto tautomerism in the excited state (ESIPT). The emission intensity of **1b** was found to be almost 1.06-fold higher than that of **2b**, indicating that strong intramolecular interactions may be responsible for the intensive emission of **1b**. The lower fluorescence intensity of **2b** may be attributed to the poor coplanarity of this molecule, which is caused by the formation of amide bonds and attachment of a new benzene group in the skeleton structure.[46] This phenyl ring may not conjugate very well with the π-system of the corresponding naphthyl groups and may not show π···π interactions with naphthalene moieties in **2b** because it is impossible to locate in the same plane. Compared to the corresponding ligand **2b**, the resulting complex **3b** exhibited almost no shift in pure DMSO ($C$ = 100 μM). The Zn complex had an emission wavelength of 505 nm, which is neither ligand-metal nor metal–ligand charge transfer. The light emission of **3b** may arise from π → π* transitions within the ligand or interligand. Complex **3b** exhibited relatively weak fluorescence, with an intensity that was 0.5-fold lower than that of **2b**. This may be due to the weaker binding of zinc ions to the ligand, which reduces the rigidity of the complex and decreases the rate of the radiative pathway of electronic excitation. In a dilute DMSO solution ($C$ = 50 μM), the fluorescence maxima were centred in the same spectral range of 425–452 and 500–503 nm with a significant enhancement (∼1.23–2.27-fold) in the fluorescence intensity for all the compounds, probably ascribable to excimer formation.

In the spectrum of these compounds in DMF ($C$ = 100 μM), the emission maxima exhibited a small blue shift ($\Delta\lambda_{max}$ = 2–5 nm) compared to that of DMSO. **1b** emitted at 426 and 499 nm in solution, and the emission bands red-shifted to 457 and 500 nm for **2b**. The emission strength of **1b** is 1.49-fold higher than that of **2b**. For the Zn complex, the emission maxima were observed at 453 and 501 nm in pure DMF, with a 0.89-fold weaker fluorescence intensity than that of the ligand. When the concentration was varied to 50 μM, enhanced intensities (1.69-fold, 1.32-fold, and 1.31-fold for **1b**–**3b**) were obtained. The emission maxima of these compounds ranged from 427 to 453 nm and from 495 to 499 nm in dilute DMF solutions.

According to the fluorescence results, the emission intensity of **1b**–**3b** decreased with increasing concentration, indicating aggregation-caused quenching (ACQ) properties. At higher concentrations, strong intermolecular π–π stacking interactions between these molecules may result in aggregate formation.[47] In Schiff bases, intramolecular proton transfer from the hydroxyl group to the imine bond occurs in either the ground (IPT) or excited (ESIPT) electronic state. The keto tautomer is more stable than the enol form in the excited state because of stabilization by intermolecular hydrogen bonding with the polar solvent molecules. The presence of a keto tautomer may also stabilize the aggregated state.[48] After photoexcitation, the most stable (*E*)-enol tautomer in the ground state absorbed UV light and reached the excited state ($S_n$) (Scheme S4). Subsequently, *cis*–*trans* conversion and excited state tautomerization occur to produce the keto structure.[49] When the (*Z*)-keto form of the molecule absorbs light, it emits fluorescence without changing its configuration in the excited singlet state.[50] The excited state energy may transfer non-radiatively to the ground state to reduce the emissions. The ground-state structures of **1b** and **2b** were observed to be present as a mixture of (*E*)-enol and (*Z*)-keto forms in pure DMSO and DMF. In **1b** and **2b**, the observed normal and tautomeric emission bands with different fluorescent behaviors may be attributed to the excited state of the *Z*-keto forms.[51] These results were in agreement with previous work,[21] which provides important information about a hydroxyamide-functionalized salen-type hybrid Schiff base 3,5-bis((*E*)-((2-hydroxybenzylidene)amino)-*N*-(2-hydroxyphenyl)benzamide).

**AIE and ACQ behavior of the compounds.** AIE is a phenomenon in which fluorophores emit weak fluorescence in dilute

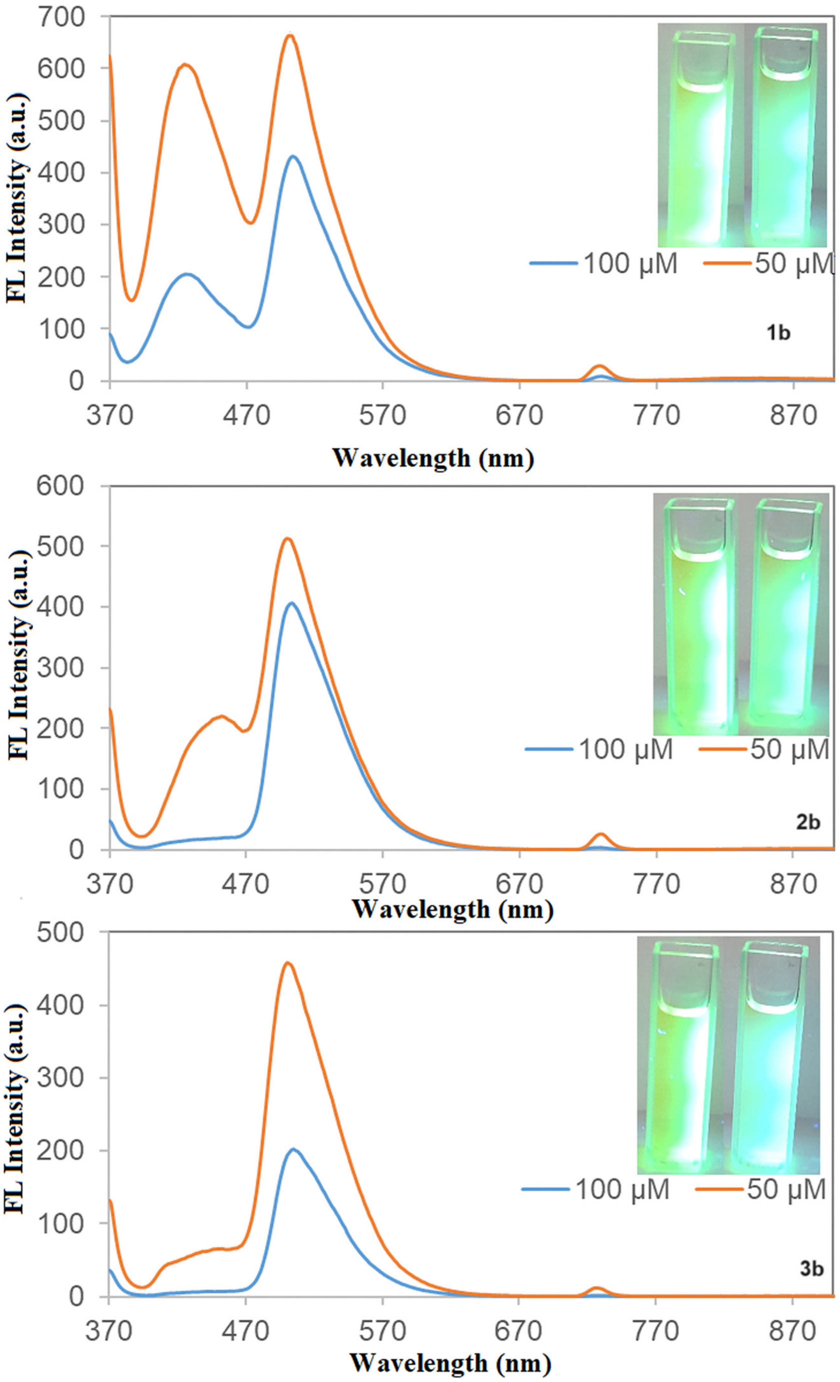

Fig. 8 Fluorescence spectra of **1b–3b** in DMSO. Inset: The photographs of the compounds after excitation.

solution but exhibit strong emission upon aggregation. Aqueous-organic mixed solvents are frequently used to trigger AIE behavior. In water-rich mixtures:

(i) Molecular solubility decreases: AIE-active molecules are generally well soluble in organic solvents but poorly soluble in water. As the water content increases, the solubility of the molecules decreases, and they tend to aggregate. This aggregation initiates the AIE effect.

(ii) Intramolecular motion becomes restricted: the aqueous environment promotes aggregation, which restricts molecular motion. The fundamental mechanism of AIE is the restriction of intramolecular rotational and vibrational motions. When molecules undergo free rotation in solution, the excited-state energy is dissipated as heat rather than light, resulting in weak fluorescence. In the aggregated state, these motions are restricted, and the energy is released as photons, producing strong fluorescence.

(iii) Fluorescence intensity increases: due to aggregation and restricted intramolecular motion, the fluorescence intensity increases significantly.

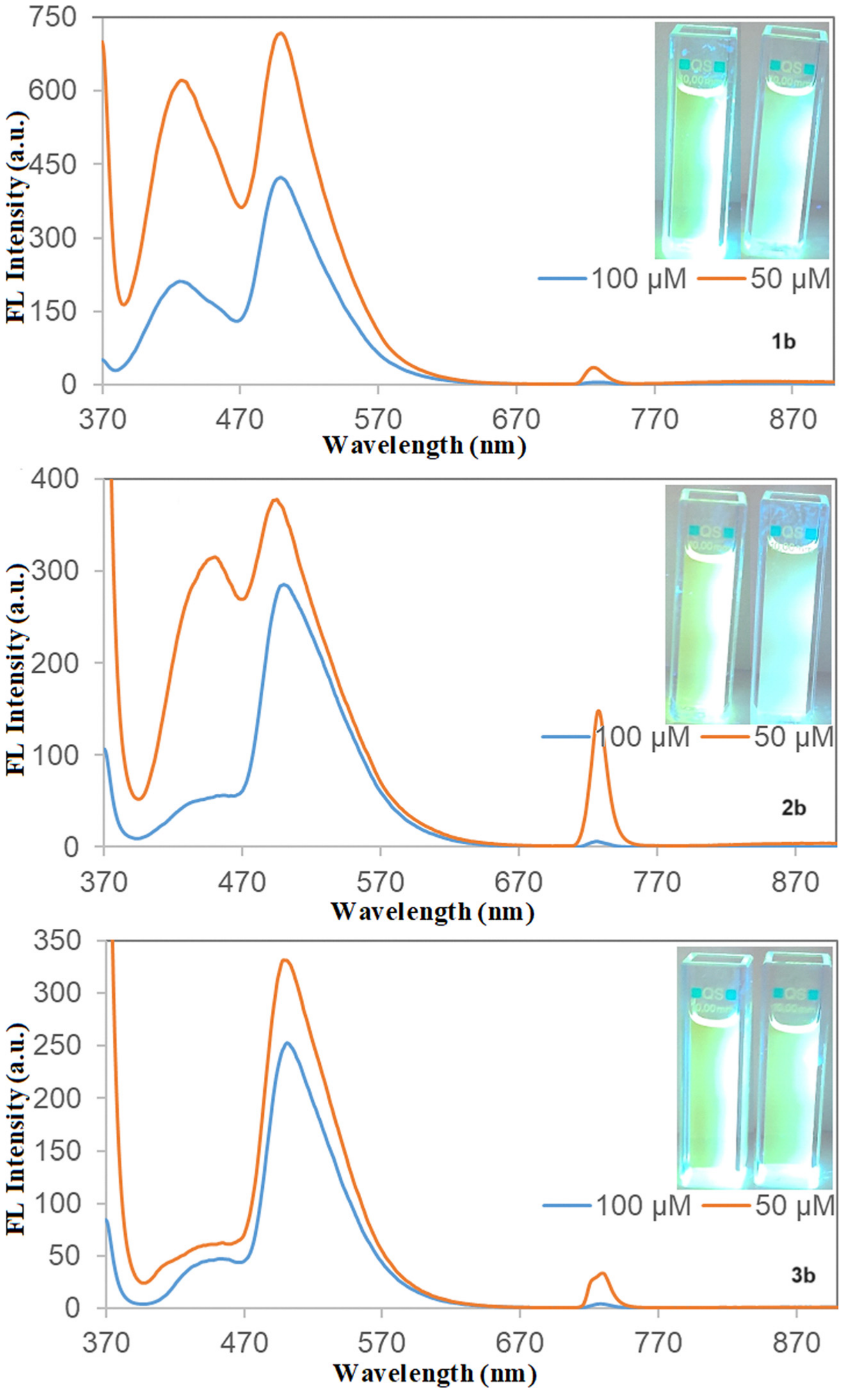

Fig. 9 Fluorescence spectra of **1b–3b** in DMF. Inset: The photographs of the compounds after excitation.

(iv) The emission wavelength may change: aggregation can alter the electronic interactions between molecules, which may cause shifts in the emission wavelength.

In fluorescent molecules that initially exhibit ACQ behavior, the transformation from ACQ to AIE can occur through metal-ion complexation. This process modifies the electronic structure of the molecule and restricts its intramolecular motions. As a result, complexation can suppress ACQ behavior and activate the AIE mechanism. In molecules showing ACQ characteristics, aggregation leads to strong π–π stacking interactions between the aromatic units. These interactions promote non-radiative decay of the excited state, resulting in fluorescence quenching. Consequently, the molecule may exhibit fluorescence in its monomeric state, whereas fluorescence is significantly quenched in the aggregated state. The main processes responsible for ACQ include: π–π stacking interactions, excimer formation, energy transfer processes and intramolecular free rotation. When the fluorescent ligand forms a complex with a metal ion, several important changes may occur:

(i) Complexation limits rotational freedom at the coordination sites, making the molecular framework more rigid. This rigidity activates the RIM mechanism, which suppresses non-radiative decay pathways. Consequently, fluorescence intensity increases.

(ii) Metal coordination can introduce steric hindrance and alter the molecular packing arrangement, making it more difficult for molecules to stack through π–π interactions. As a result, the π–π stacking interactions responsible for ACQ are reduced.

(iii) Upon complexation, molecules may adopt different aggregation patterns, such as J-type aggregates or loosely packed aggregates. These aggregation modes are less likely to cause fluorescence quenching and may even enhance emission in AIE-active systems.

(iv) Metal complexation can modify the electronic transitions of the system such as ICT (intramolecular charge transfer) and MLCT (metal–ligand charge transfer). These electronic effects can increase the probability of radiative transitions, thereby improving the fluorescence quantum yield.

Fluorophores can exhibit different emission behaviors in water owing to their high polarity and ability to form H-bonds. Therefore, the AIE and ACQ emission properties of the compounds were investigated in polar protic aqueous solutions. For this, DMSO and DMF solutions of **1b–3b** with water fractions ($f_w$) of 10–90% were prepared, and their emission was measured after overnight incubation to ensure that the formation of a stable aggregate was fully completed. As shown in Fig. 10, **1b** exhibited two fluorescence maxima at 428 and 498 nm at 10% water content in DMSO. These emission bands disappeared with the appearance of a new broad emission band in the range of 443–448 nm until 80% fraction, while two maxima were observed again at 420 and 442 nm at 90% fraction. **1b** displayed very strong fluorescence in the DMSO–$H_2O$ binary solvent mixture, although it had much less intense fluorescence in pure DMSO. Its emission intensity increased with increasing proportion of water, indicating aggregation-induced emission in an aqueous DMSO solution.[52] When the volume ratio of water was 30%, the intensity reached the maximum value.

The fluorescence maxima of **2b** exhibited small shifts to 458–449 nm and 502–504 nm in the range of 10–60% fraction, which depends on the polarity of the medium. Upon increasing the solvent polarity (10–50% fraction), a slight increase was

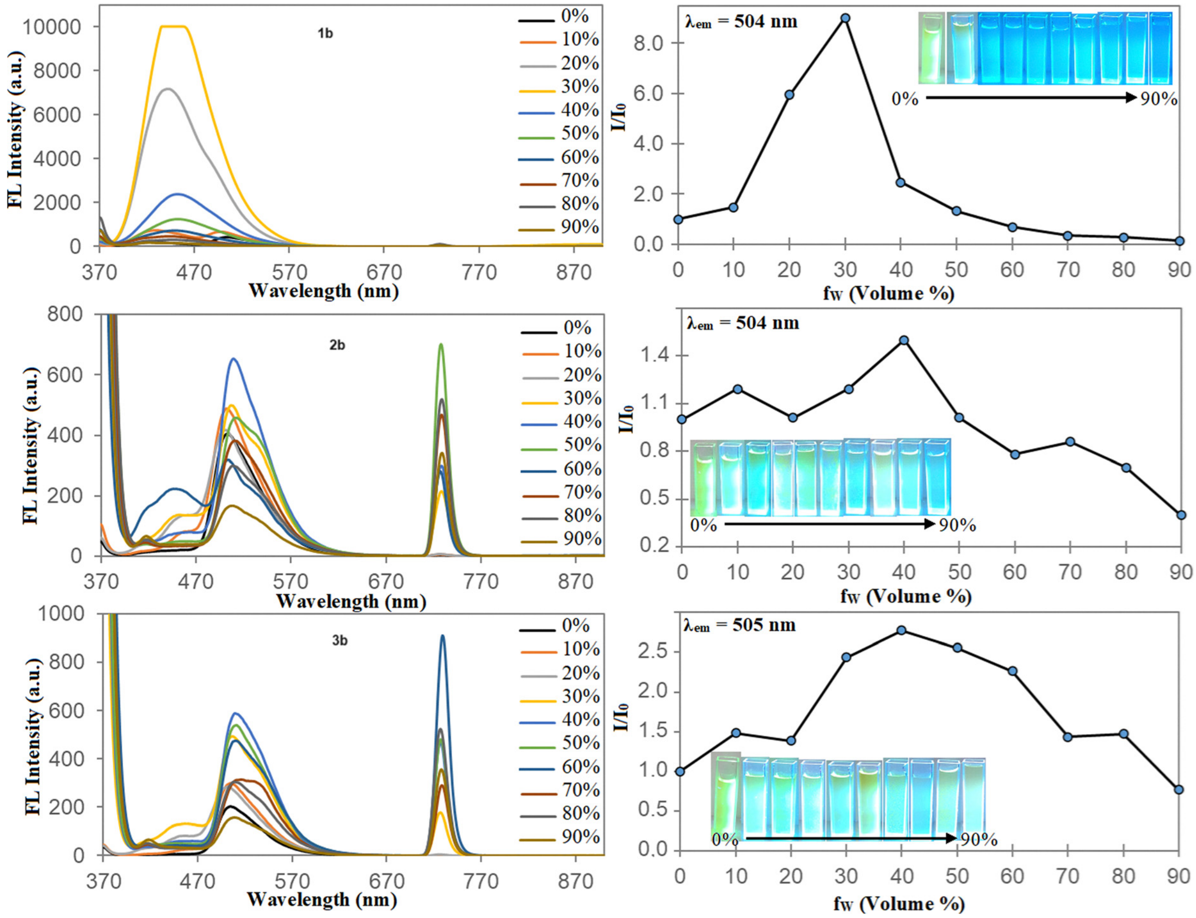

Fig. 10 Fluorescence spectra of **1b–3b** in DMSO–$H_2O$ mixtures at different water fractions after overnight incubation. Plots of fluorescence intensity ($I/I_0$) *versus* water fraction ($f_w$) Inset: The photographs of the samples with increasing $f_w$ illuminated under 365 nm.

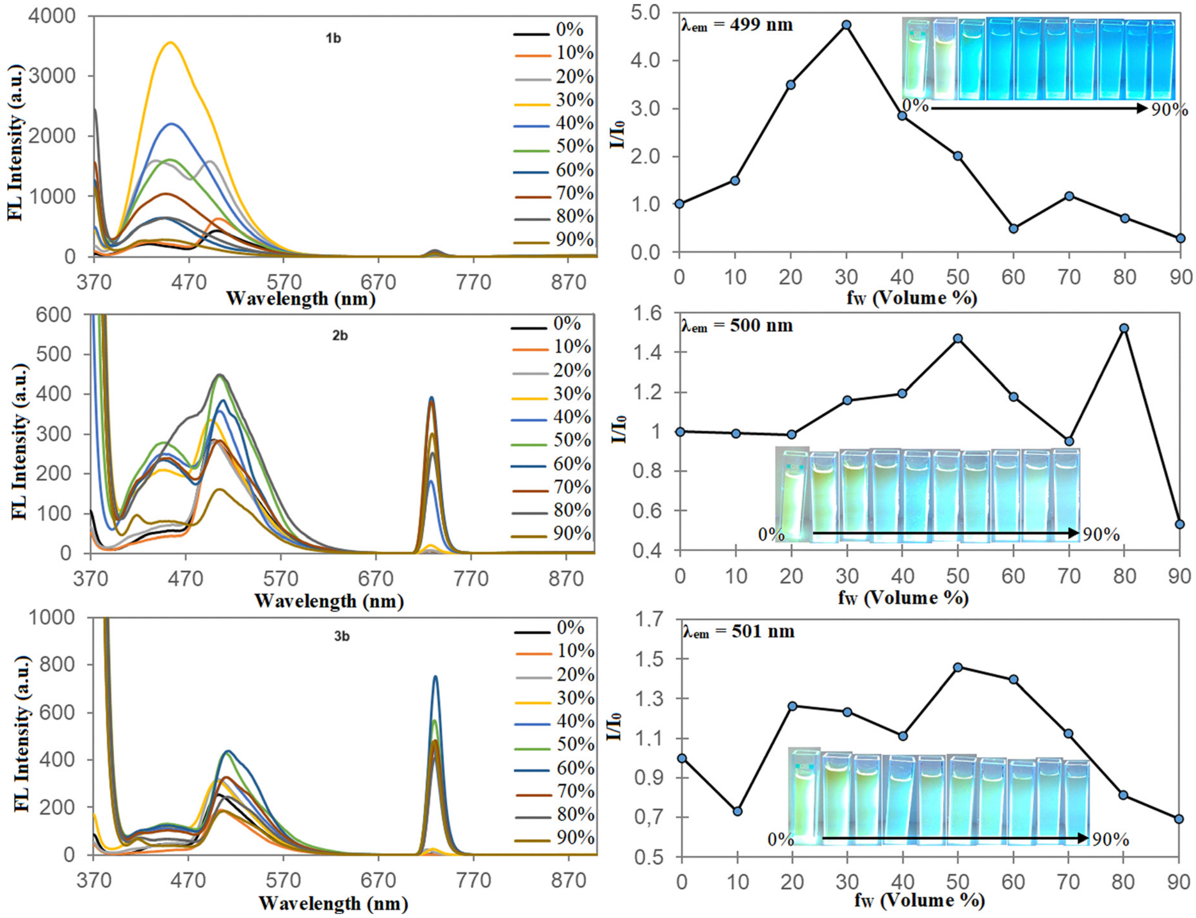

Fig. 11 Fluorescence spectra of **1b–3b** in a DMF–$H_2O$ mixture at different water fractions after overnight. Plots of fluorescence intensity ($I/I_0$) *versus* water fraction ($f_w$) Inset: The photographs of the samples with increasing $f_w$ illuminated under 365 nm.

obtained in the emission intensity as compared to that in pure DMSO solution. This was followed by a weak emission intensity shoulder ($\lambda_{em}$ = 417–418 nm) and maximum ($\lambda_{em}$ = 511–509 nm) until 90% content. In complex **3b**, the maximum of the fluorescence band was seen at 504 nm at 10% water fraction and then shifted to the red area by 3–12 nm. A new hump was seen at 456–458 nm within the 20–40% fraction range, and blue shifted to 417–418 nm in 50–90% aqueous DMSO solution. The maximum fluorescence intensity was obtained at 40% water fraction for both **2b** and **3b**, because of maximal aggregate formation.

Similar results were obtained for the aqueous DMF solution. **1b–3b** exhibited intensive emission in the binary solvent mixture, which indicates that the polarity of the medium has the same effect on these molecules. The maximum emission intensity was observed at 30%, 50%, and 60% water fraction for **1b–3b**, respectively. As depicted in Fig. 11, the fluorescence maxima of **1b** were around at 428–436 and 500–492 nm for two water fractions of DMF (10–20%). These bands were absent, and a new broad maximum was observed between 451 and 446 nm in the region of 30–80% fraction, while a new maximum appeared at 422 nm at 90% water fraction. The ligand and Zn(II) complex had two emission maxima ($\lambda_{em}$ = 447–456 and 496–510 nm for **2b**, and 445–458 and 504–511 nm for **3b**) in all water fractions of DMF. As well, they emitted a weak intensity band ($\lambda_{em}$ = 416–420 nm) at 80–90% fraction.

The above results confirmed that **1b–3b** show AIE behavior in a solvent–$H_2O$ binary mixture, due to the existence of strong intermolecular H-bonding interactions. When $f_w$ increases, the molecules form aggregates by electrostatic interactions. Increasing the solvent polarity may cause the transformation of these compounds from the excited state to the twisted intramolecular charge transfer state.[53] Increasing water content increases the restriction of intramolecular rotation in the aggregated state of these compounds, because of decreasing their solubility.[54] The isolated dimer formation in aqueous solution can lead to an increase in the loss of energy *via* the radiative path and enhance their fluorescence intensity.[55] In Schiff bases, the C=N bond isomerization and intramolecular rotation inhibit the ESIPT process. The intramolecular motions, including free rotation and vibration of the C=N group and aromatic ring in the molecular structure, promote non-radiative decay, which dominates leading to low emission. The aggregated state activates the ESIPT because of the restriction of intramolecular rotation, which contributes to strong fluorescence enhancement. In summary, an aqueous–organic medium decreases the solubility of compounds **1b–3b**, which

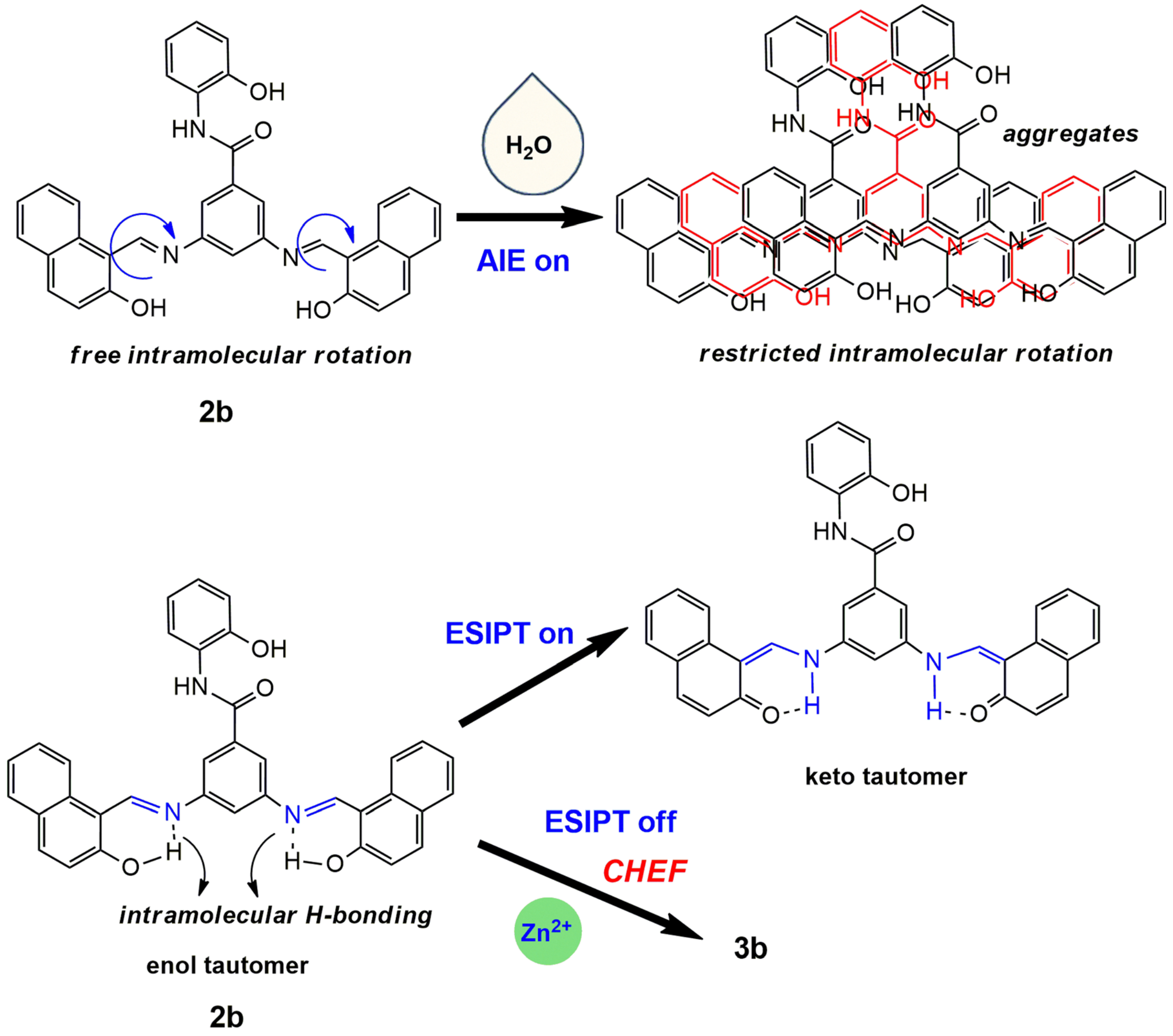

Scheme 2 Proposed mechanistic pathway for ESIPT and AIE behaviours of **2b**.

promotes aggregation and restricts intramolecular motion. As a result, the AIE fluorescence was significantly enhanced in this medium. For zinc complex **3b**, the more rigid molecular structure leads to restricted intramolecular motions, decreased π–π stacking interactions and reduced non-radiative energy dissipation. As a result, the initially ACQ-dominant system was transformed into an AIE-active system, leading to enhanced fluorescence in the aggregated state (Scheme 2). The AIE-fluorescent behavior of **3b** was also compared with those Zn-MOFs, and the data are listed in Table 3. This property is particularly important for several potential applications:

(i) Fluorescent sensing of metal ions: the prepared Schiff bases **1b**–**2b** can act as a selective metal ion receptor due to the strong enhancement of emission upon chelation.

(ii) Bioimaging: bright AIE in aqueous or aggregated environments can allow cell or tissue imaging with reduced background fluorescence compared to ACQ-prone fluorophores.

(iii) Optoelectronic materials: the RIR- and ESIPT-mediated emission can be leveraged in solid-state lighting or AIE-active OLEDs.

**CIE 1931 chromaticity diagrams.** Chromaticity diagrams were obtained using the color calculator software.[71] As presented in Table 4, the chromaticity coordinates ($x/y$) of **1b** were 0.1765/0.3757 and 0.1661/0.2632, falling between the bluish-green and greenish-blue regions of the diagram at 100 μM and 50 μM concentrations in DMSO (Fig. 12a). The coordinates ($x/y$ = 0.1699/0.3445 and 0.1653/0.2614) lie in the bluish-green and greenish-blue regions in DMF (Fig. 12b). In these solutions, **1b** has a moderate correlated color temperature (CCT) value (10 000–20 000 K) at a 100 μM concentration, but it displays very high CCT > 40 000 K at a 50 μM concentration, classified as a 'cool' light source.[72] The coordinates ($x/y$ = 0.1879/0.5831 and 0.1769/0.4889) of **2b** are close to the green region of the diagram in DMSO. These coordinates are observed in the green and greenish-blue regions in DMF. **2b** has a moderate CCT < 10 000 K at 100 μM concentration of DMSO and DMF, which may be described as a 'warm' light source.[73] The correlated color temperature value increased with a decrease in concentration, and was calculated to be in the range of ∼10 000 K to 41 000 K. **3b** has the coordinates ($x/y$ = 0.1867/0.6042 and

Table 3 Comparison of **3b** with other Zn-MOFs

| MOFs structure | Ligand | Media | Emission-characteristics | Ref. |
|---|---|---|---|---|
| $[Zn(L^1)_2Cl_2]$ | 1-Methylbenzimidazo-2-yl-methyleneaniline | Solid | Green luminophores, red luminophore | 1 |
| $[Zn(L^2)_2Cl_2]$ | 1-Ethyl-2-(4-methoxyphenyl)azobenzimidazole | | | |
| $[Zn(Titpe)(bcpf)\cdot(DMF)]_n$ | 1,1,2,2-Tetrakis(4-(1*H*-imidazol-1-yl)phenyl)ethane<br>4,4′-Sulfonyldibenzoic acid | Solid | Blue fluorescence, LLCT | 56 |
| $[KZn(3\text{-}MeOsalpn)(\mu_{1,1}\text{-}NCS)]_2$ | *N*,*N*′-Bis(2-hydroxy-3-methoxybenzylidene)-propane-1,2-diamine | Solid | Weak-fluorescent | 57 |
| | | DMSO | Fluorescent, CHEF | |
| $[Zn(L)]_n$ | 3,6-Bis(1,10-phenathroline-[5,6-*d*]imidazole-2-yl)carbazole | Solid | Orange fluorescence | 58 |
| | | DMSO | Blue fluorescence CHEF | |
| $[Zn_5(L)_2]\cdot 2H_2O$ | *N*,*N*-Bis(3-ethoxysalicylidene)hydrazine | Solid | Red fluorescence, AIE | 59 |
| | | MeOH | Non-emissive | |
| $[ZnL_2Cl_2]$ | (3-(4-5-(4-Chlorophenyl)diazenyl)-2-hydroxybenzylideneamino)<br>((Phenylimino)methyl)-4*H*-chromen-4-one | DMSO | Fluorescent, CHEF | 60 |
| $[Zn(L)_2]$ | 2-{(*E*)-[(3,4-Dimethylphenyl)imino]methyl}-5-[(*E*)-Phenyldiazenyl]phenol | DMF | Fluorescent, CHEF | 61 |
| $[ZnLCl(Ts)]$ | *N*-[2-(5,6-Dihydrobenzimidazo[1,2-*c*]quinazoline-6-yl)phenyl]-4-methylbenzolsulfamide | Solid | Fluorescent | 62 |
| | *p*-Tolylsulfonyl | $CH_3CN$<br>EtOH | Weak-fluorescent | |
| $[Zn(L)_2][N_2O_6\cdot 2(H_2O)]$ | (*E*)-4-(((8-(4-Chlorophenyl)-3-isobutyl-3*H*-imidazo [4′,5′:3,4]Benzo[1,2-*c*]isoxazol-5-yl)imino)methyl)phenol | MeOH | Fluorescent | 63 |
| $[Zn_2(L)_2(H_2O)_2]\cdot 2DMF$ | 3-[(5-Chloro-2-hydroxy-benzylidene)-amino]-4-hydroxy-chromen-2-one | DMSO | Fluorescent, CHEF | 64 |
| $[Zn_2(L)_2\cdot(4,4'\text{-}bpy)_2]_n$ | 4,4′-Bipyridine | | Weak-fluorescent | |
| $[(Zn_2(o\text{-}van\text{-}gly)(phen)OAc)_2]\cdot 3MeOH$ | Potassium 2-((2-hydroxy-3-methoxybenzylidene)amino)acetate<br>1,10-Phenanthroline | Solid | Fluorescent, LLCT | 65 |
| $[Zn(L)Cl_2]$ | 4-Methoxy-*N*-(pyridin-2-ylmethylene)aniline | Solid | Fluorescent, LLCT | |
| $[Zn(L)Cl_2]\cdot CH_3CN$ | 4-Methoxy-*N*-(quinolin-8-ylmethylene)aniline | $CH_3CN$ | TICT | 66 |
| $[ZnDyL(NO_3)_2(OAc)(CH_3OH)](CH_3OH)_3$ | Bis(5-bromine-3-methoxysalicylidene)-3-oxapentane-1,5-diamine | Solid | Fluorescent, CHEF | 67 |
| $[Zn_2L_2(\mu_{1,1}\text{-}N_3)(N_3)]$<br>$[ZnL(NCO)(H_2O)]$<br>$[ZnL(NCS)(H_2O)]$ | (((*E*)-2-Ethoxy-6-((quinolin-8-ylimino)methyl)phenol)) | DMF | Weak-fluorescent | 68 |
| $[ZnL_2]$ | Potassium(*E*)-3-hydroxy-2((2-hydroxy-4(tetradecycloxy)benzylidene)amino)butanoate | DMSO | Fluorescent, CHEF | 69 |
| $[ZnL_2]$ | (*E*)-1-(4-Fluorophenyl)-*N*-(1,10-phenanthrolin-5-yl)methanimine | EtOH | Fluorescent | 70 |
| $[Zn_2L_2(H_2O)_2]\cdot 2H_2O$ | 3,5-Bis((*E*)-((2-hydroxynaphthalen-1-yl)methylene)amino)-*N*-(2-hydroxyphenyl)benzamide | DMSO<br>DMF | Bluish-green/green fluorescence, AIE | This work |

LLCT: ligand-to-ligand charge transfer; TICT: twisted intramolecular charge transfer.

0.1692/0.3568) in DMSO, which fall in the green and bluish-green regions of the diagram, while it appears in the green region in DMF. The CCT of **3b** ranging from 8300 K to 15 700 K, significantly increased with a reduction in the concentration in DMSO. A CCT ~ 10 000 K may be referred to as a 'cool' light source.

The color purity of **1b–3b** was obtained using eqn (6):[74]

$$\%\ \text{color purity} = \frac{\sqrt{(x_s - x_i)^2 + (y_s - y_i)^2}}{\sqrt{(x_d - x_i)^2 + (y_d - y_i)^2}} \times 100 \qquad (6)$$

Here ($x_i/y_i$) are the coordinates of the illuminant, ($x_s$, $y_s$) are the coordinates of the sample, and ($x_d/y_d$) are the coordinates of the dominant emission wavelength.

Table S3 shows that diimine **1b** had the lowest color purity values (~33–40%) at a 100 μM concentration in DMSO and DMF. The color purity reached to ~38–45% with a decrease of the concentration. Amido-Schiff base **2b** has a moderate color purity at a 100 μM concentration in DMSO and DMF, which ranges from ~65–66% to ~49–51%. The purity values of **2b** decreased to 58–49% at a 50 μM concentration. The color purity of complex **3b** was found to be ~68–67% at a 100 μM concentration in DMSO, while it decreased sharply to 38% at a 50 μM concentration. The purity values were calculated to be ~51–52% and ~53–54% in DMF. Consequently, it was concluded that the color purity values increased in the order **1b** < **2b** < **3b** in both DMSO and DMF.

**DPPH radical scavenging activity.** DPPH is a stable free nitrogen radical that displays a purple color in solution. When the DPPH radical accepts a hydrogen atom from the scavenger molecule, its color turns yellow, with a reduction in absorbance at 517 nm.[75]

Free radical scavenging was studied in DMSO at a set concentration of DPPH (50 μM). Absorbance was measured at 517 nm after incubation for 30 min in the dark. Ascorbic acid

Table 4 The chromaticity diagram parameters of compounds **1b–3b**

| | **1b** | | **2b** | | **3b** | |
|---|---|---|---|---|---|---|
| | Color coordinates | | Color coordinates | | Color coordinates | |
| Media | *x*<br>*y* | CCT (K) | *X*<br>*Y* | CCT (K) | *x*<br>*y* | CCT (K) |
| DMSO (100 μM) | 0.1765<br>0.3757<br>Bluish-green | 13 789.67 | 0.1879<br>0.5831<br>Green | 8501.71 | 0.1867<br>0.6042<br>Green | 8352.8 |
| DMSO (50 μM) | 0.1661<br>0.2632<br>Greenish-blue | 41 067.32 | 0.1769<br>0.4889<br>Green | 10 028.77 | 0.1692<br>0.3568<br>Bluish-green | 15 689.55 |
| DMF (100 μM) | 0.1699<br>0.3445<br>Bluish-green | 16 751.15 | 0.1918<br>0.4675<br>Green | 9878.91 | 0.1822<br>0.4773<br>Green | 10 056.01 |
| DMF (50 μM) | 0.1653<br>0.2614<br>Greenish-blue | 42 861.63 | 0.1711<br>0.2609<br>Greenish-blue | 41 029.34 | 0.1778<br>0.4598<br>Green | 10 603.59 |

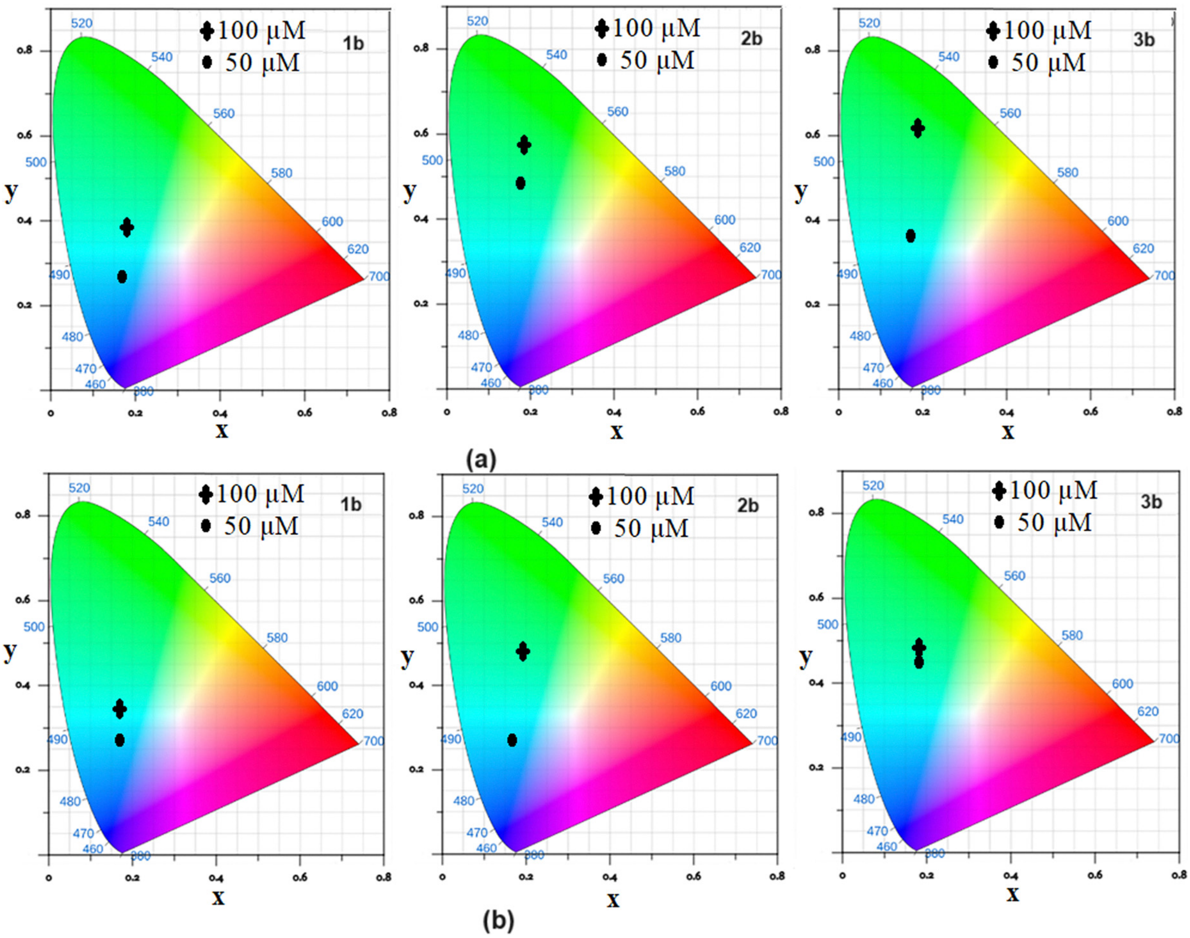

Fig. 12 CIE-1931 chromaticity diagrams of **1b–3b** in (a) DMSO and (b) DMF.

was used as the standard for comparison. As seen in Fig. S24, **1b–3b** showed dose-dependent scavenging activity in solution. A lower concentration of the compounds in the free radical solution displayed low antioxidant potential (1.39–3.94%), but DPPH radicals were scavenged in the range of percentage 9.38–28.91% upon increasing the concentration from 12.5 to 75 μM.

According to the results, the inhibition decreased in the order **2b** > **1b** > **3b**. **1b** and **2b** exhibited relatively higher potency than **3b**, which may be due to the presence of active hydroxyl groups for DPPH scavenging. **2b** was found to be more active than diimine **1b**, whose formula lacks an extra hydroxyl group in the phenyl ring. Moreover, all compounds showed weak activity compared to ascorbic acid.

***In silico* ADME results.** Some physicochemical parameters, such as molecular weight (MW), number of heavy atoms, ratio of sp$^3$ hybridized carbon atoms (F. $C_{\mathrm{sp}^3}$), number of rotatable bonds, hydrogen bond acceptors (HBA) and donors (HBD), molar refractivity (MR), topological polar surface area (TPSA), lipophilicity and water solubility, and absorption, distribution, metabolism, and excretion (ADME) properties of molecules can be obtained using the *in silico* SwissADME web browser at https://www.swissadme.ch.[76,77] The partition coefficient ($\log P_{\mathrm{o/w}}$) was used as a descriptor for lipophilicity (o: *n*-octanol, w: water). Solubility is one of the main factors affecting absorption. The $\log S$ scale was as follows: insoluble < −10 < poorly < −6 < moderately < −4 < soluble < −2 very < 0 < highly. The *in silico* SwissADME method provides free access to evaluate the drug-likeness potency of molecules because of the relationship between physicochemical and pharmacokinetic parameters according to the directions of the Lipinski, Ghose, Veber, Egan, and Muegge filters. Lipinski's rule of five: (i) MW $\leq$ 500, (ii) $M\log P \leq 5$, (iii) HBA $\leq$ 10, (iv) HBD $\leq$ 5. This rule is called the Rule of 5′, because the border values are 500, 5, 2 × 5, and 5.[78] Ghose filter: (i) 160 $\leq$ MW $\leq$ 480; (ii) $-0.4 \leq W\log P \leq 5.6$; (iii) 40 $\leq$ MR $\leq$ 130; (iv) 20 $\leq$ atoms $\leq$ 70. Veber filter: (i) rotatable bonds $\leq$ 10, (ii) TPSA $\leq$ 140. Egan filter: (i) $W\log P \leq 5.88$, (ii) TPSA $\leq$ 131.6. Muegge filter: (i) MW $\leq$ 500, (ii) $M\log P \leq 4.15$, (iii) HBA $\leq$ 10, (iv) HBD $\leq$ 5. Ghose filter: (i) 200 $\leq$ MW $\leq$ 600; (ii) $-2 \leq X\log P \leq 5$; (iii) TPSA $\leq$ 150; (iv) Num. rings $\leq$ 7; (v) Num. carbon > 4; (vi) Num. heteroatoms > 1 and (vii) Num. Rotatable bonds $\leq$ 15; (viii) HBA $\leq$ 10; (ix) HBD $\leq$ 5.

The bioavailability radar contains physicochemical properties, such as flexibility (rotatable bonds), insaturation ($C_{\mathrm{sp}^3}$), insolubility ($\log S$), polarity (TPSA), size (MW), and lipophilicity (XLOGP3). The pink area of the radar includes the optimal range for each property (−0.7 < XLOGP3 < +5.0; 150 < MW < 500; 20 Å$^2$ < TPSA < 130 Å$^2$; 0 < $\log S$ < 6; 0.25 < $C_{\mathrm{sp}^3}$ < 1; 0 < rotatable bonds < 9).[79] The BOILED-Egg graphical model deals with human gastrointestinal absorption (HIA) and blood–brain barrier (BBB) permeation, which are according to the white and yellow (yolk) regions, respectively. This method uses XLOGP3 and TPSA as the lipophilicity and polarity descriptors, respectively. The white region showed a high probability of passive absorption by the gastrointestinal tract, whereas the yolk region exhibited a high probability of brain penetration. The blue and red points are related to the *P*-glycoprotein substrate (PGP$^+$) and non-substrate (PGP$^-$), respectively.

As shown in the ADME profiles in Tables S4 and S5, compounds **1b–2b** have a number of HBA groups 6 and HBD groups 3–4. The MR value was found to be within the range of 139 and 169, while the TPSA was calculated to be less than 115 Å$^2$. Lipophilicity was found to be in the following order: **2b** > **1b**, owing to the consensus $\log P_{\mathrm{o/w}}$. All compounds are poorly soluble in water and have low HIA properties, but cannot pass through the blood–brain barrier. Organic compounds **1b** and **2b** were found to be non-substrates of *P*-glycoprotein (PGP$^-$) and non-inhibitors of cytochrome P450 (CYP) liver isoenzymes. These compounds agreed with Veber's and Lipinski's rules, except for molecular weight (>500 for **2b**). Violation is related to the physicochemical properties of the molecules, which are outside the range of filters. It has been suggested that molecules violating more than one of these rules may have problems with bioavailability. If the molecule provides at least three out of the five rules, its GI absorption is likely to improve. For **1b–2b**, the bioavailability score was found to be 0.55–0.56, indicating the probability (%10) for use as an oral drug in rats with respect to drug-likeness. PAINS and Brenk filters are chemically reactive, metabolically unstable, and toxic fragments of the molecule. The obtained synthetic accessibility scores (3.31–3.69) implied a relatively difficult synthesis of compounds **1b–2b.**

The Bioavailability Radar is shown in Fig. S25a–c. As shown in this figure, some descriptors fell outside the pink area of the radar. These compounds are not suggested to be orally bioavailable because of their lipophilic, insoluble, and unsaturated properties. The molecular size of **2b** was higher than 500 g mol$^{-1}$. The BOILED-Egg graphs show that they fall outside this range, indicating no GI absorption and BBB penetration ability. Organic compounds **1b** and **2b** are non-substrates for *P*-glycoprotein (PGP$^-$).

The computational ADME analysis suggests that these compounds exhibit limited water solubility and reduced gastrointestinal (GI) absorption, which may impede their oral bioavailability. Several deviations from commonly used drug-likeness criteria, including the Ghose, Egan, and Muegge rules, were also observed, indicating that the molecule does not fully conform to standard physicochemical parameters typically associated with orally active drugs. These limitations are likely a consequence of the large molecular size and extended π-conjugated system, which increase lipophilicity and hinder solubility in aqueous media. Nonetheless, such deviations are not uncommon for structurally complex or highly conjugated molecules, many of which retain significant biological activity despite low drug-likeness scores. Optimization strategies, such as structural modification or advanced formulation techniques, may be necessary to improve solubility, absorption, and overall pharmacokinetic performance.

## Conclusions

In this work, an amido-Schiff base, 3,5-bis((*E*)-((2-hydroxynaphthalen-1-yl)methylene)amino)-*N*-(2-hydroxyphenyl)benzamide (**2b**), was produced by the amidation reaction between Schiff base **1b** and 2-hydroxyaniline. Dimeric and homo-dinuclear complex **3b** has a 2 : 2 molar ratio of the ligand Zn$^{2+}$. Their structures were established using infrared (IR) spectroscopy, nuclear magnetic resonance (NMR) spectroscopy, mass and UV-vis spectroscopies, and elemental analyses. According to the microanalysis and mass data, dinuclear zinc complex **3b** possesses a $[Zn_2L_2(H_2O)_4]\cdot 2H_2O$ composition with a distorted octahedral geometry. The IR and NMR spectral data showed the coordination of naphtholic oxygen and imino nitrogen atoms with the central metal ion. TGA and molar conductance measurements revealed the thermal stability and nonelectrolytic nature of **3b**.

The experimental results indicated that organic compounds **1b**–**2b** were present in the enol form in the solid state, whereas their structures were more stable in the keto form in solution. DFT analysis strongly supports the experimental findings. The calculated IR, NMR, and UV-vis data confirmed the structural features and photophysical properties of the molecules. The presence of N···H–O and N–H···O hydrogen bonds in the enol and keto forms, validated by geometry optimization, underpins the observed spectral characteristics and absorption properties. Furthermore, the correlation between the calculated and experimental band gaps solidifies our understanding of the electronic behavior of **1b**–**3b** and provides insights into the tuning of the optical properties through metal complexation.

Upon irradiation at 365 nm, **1b**–**3b** was fluorescent in both DMSO and DMF solutions at room temperature. These compounds are green or bluish-green/greenish-blue fluorophores, respectively. Their emissive states are attributed to intraligand charge transfer transitions. The position and intensity of the emission bands were evaluated depending on their structures and concentrations, which influence the release of absorbed energy through nonradiative decay. The fluorescence emission intensity of **1b** was higher than that of **2b** in the pure solvents. The dual emission of the free molecules exhibited typical ESIPT characteristics in the solution. The emission brightness of ligand **2b** decreased upon coordination with the zinc ions. The ACQ effect was observed at high concentrations, whereas the intensity increased in a mixture of solvent–$H_2O$ with varying water fractions ($f_w$ = 0–90%) because of their AIE properties.

The physicochemical and pharmacokinetic ADME (absorption, distribution, metabolism, and excretion), drug-likeness, medicinal chemistry, and related parameters of the synthesized compounds were calculated using the SwissADME login-free website. **1b**–**2b** had high lipophilicity but poor solubility in water. They have low human intestinal absorption and are unable to cross the blood–brain barrier (BBB). Ligands cannot act as *P*-glycoprotein substrates or inhibit cytochrome P450 enzymes. They provide Veber's rules (rotatable bonds and TPSA), but violate some rules (Lipinski, Ghose, Egan and Muegge). Their bioavailability score (0.55–0.56) possesses good drug-likeness properties.

## Author contributions

Conceptualization, Ö. G. and S. K.; methodology, Ö. G.; investigation, Ö. G.; visualization, Ö. G.; validation, Ö. G.; software, G. J. and S. K.; writing – original draft, Ö. G., G. J. and S. K.; writing – review and editing, Ö. G. All authors have read and agreed to the published version of the manuscript.

## Conflicts of interest

The authors declare no conflicts of interest.

## Data availability

Additional documents are included in the supplementary information (SI). This supplementary information file contains theoretically calculated IR, NMR, and UV-GB spectra of compounds in the gas phase, as well as spectra recorded in solution, Tauc and ASF graphs, antioxidant activity and bioavailability radar plots, and some tables and schemes related to enol–keto tautomerism. See DOI: https://doi.org/10.1039/d6nj00512h.

## Acknowledgements

Özlem Güngör is grateful to Prof. Metin Gürü, Prof. Fatih Akkurt, Prof. Atilla Murathan and Assist. Prof. Levent Nuralın for allowing her to use a fluorescence spectrophotometer. This paper is dedicated to the 103rd anniversary of the Republic of Turkey.

## References

1 S. E. Korolenko, K. P. Zhuravlev, V. I. Tsaryuk, A. S. Kubasov, V. V. Avdeeva, E. A. Malinina, A. S. Burlov, L. N. Divaeva, K. Y. Zhizhin and N. T. Kuznetsov, *J. Lumin.*, 2021, **237**, 118156, DOI: 10.1016/j.jlumin.2021.118156.
2 A. S. Burlov, V. G. Vlasenko, Yu. V. Koshchienko, N. I. Makarova, A. A. Zubenko, Yu. D. Drobin, L. N. Fetisov, A. A. Kolodina, Ya. V. Zubavichus, A. L. Trigub, S. I. Levchenkov and D. A. Garnovskii, *Polyhedron*, 2018, **154**, 65–76, DOI: 10.1016/j.poly.2018.07.034.
3 M. Arshad, J. R. At, V. Joseph and A. Joseph, *J. Lumin.*, 2023, **258**, 119818, DOI: 10.1016/j.jlumin.2023.119818.
4 A. B. Velappan, A. Husain, N. Rajendran, B. Ghazal and S. Makhseed, *J. Mol. Liq.*, 2022, **359**, 119273, DOI: 10.1016/j.molliq.2022.119273.
5 K. Bamnavat, V. Bhardwaj, T. Anand, S. K. A. Kumar and S. K. Sahoo, *Dyes Pigm.*, 2021, **184**, 108844, DOI: 10.1016/j.dyepig.2020.108844.
6 Z. Wu, J. Xu, Z. Wu, R. Zhao and L. Hou, *J. Photochem. Photobiol., A*, 2024, **453**, 115668, DOI: 10.1016/j.jphotochem.2024.115668.
7 V. Bhardwaj, K. Bhardwaj and S. K. Sahoo, *J. Fluoresc.*, 2023, **33**, 1157–1164, DOI: 10.1007/s10895-022-03138-3.
8 B. Kupcewicz, A. Kaczmarek-Kedziera, K. Lux, P. Mayer and E. Budzisz, *Polyhedron*, 2013, **55**, 259–269, DOI: 10.1016/j.poly.2013.03.035.

9 T. Dziembowska, M. Szafran, A. Katrusiak and Z. Rozwadowski, *J. Mol. Struct.*, 2009, **929**, 32–42, DOI: 10.1016/j.molstruc.2009.04.001.

10 A. K. Satapathya, S. K. Behera, A. Yadav, L. N. Mahour, C. V. Yelamaggad, K. L. Sandhya and B. Sahood, *J. Lumin.*, 2019, **210**, 371–375, DOI: 10.1016/j.jlumin.2019.02.056.

11 A. Mandal, D. Fitzmaurice, E. Waghorne, A. Koll, A. Filarowski, S. Quinn and S. Mukherjee, *Spectrochim. Acta, Part A*, 2004, **60**, 805–813, DOI: 10.1016/S1386-1425(03)00305-6.

12 P. Acosta-Guzmán, A. Ojeda-Porras and D. Gamba-Sáncheza, *Adv. Synth. Catal.*, 2023, **365**, 4359–4391, DOI: 10.1002/adsc.202301018.

13 A. K. Manna, M. Sahu, K. Rout, U. K. Das and G. K. Patra, *Microchem. J.*, 2020, **157**, 104860, DOI: 10.1016/j.microc.2020.104860.

14 A. K. Manna, J. Mondal, K. Rout and G. K. Patra, *J. Photochem. Photobiol., A*, 2018, **367**, 74–82, DOI: 10.1016/j.jphotochem.2018.08.018.

15 S. Ghosh, Md. A. Alam, A. Ganguly and N. Guchhait, *Spectrochim. Acta, Part A*, 2015, **149**, 869–874, DOI: 10.1016/j.saa.2015.04.025.

16 M. Mishra, K. Tiwari, A. K. Singh and V. P. Singh, *Inorg. Chim. Acta*, 2015, **425**, 36–45, DOI: 10.1016/j.ica.2014.10.026.

17 M. Nemakal, Giddaerappa, Shantharaja, V. A. Sajjan and L. K. Sannegowda, *J. Electroanal. Chem.*, 2021, **898**, 115657, DOI: 10.1016/j.jelechem.2021.115657.

18 S. Abbas, S. Afzal, H. Nadeem, D. Hussain, P. Langer, J. Sevigny, Z. Ashraf and J. Iqbal, *Bioorg. Chem.*, 2022, **118**, 105456, DOI: 10.1016/j.bioorg.2021.105456.

19 D. Śmiłowicz and N. Metzler-Nolte, *J. Inorg. Biochem.*, 2020, **206**, 111041, DOI: 10.1016/j.jinorgbio.2020.111041.

20 P. ReddyPrasad and T. Imae, *J. Taiwan Inst. Chem. Eng.*, 2017, **72**, 194–199, DOI: 10.1016/j.jtice.2017.01.009.

21 Ö. Güngör, *Inorg. Chim. Acta*, 2025, **574**, 122410, DOI: 10.1016/j.ica.2024.122410.

22 A. Benhassine, M. I. Chouiter, M. Kara-Ali, N. Kacem-Chaouche, H. Merazig and A. Belfaitah, *J. Mol. Struct.*, 2023, **1294**, 136261, DOI: 10.1016/j.molstruc.2023.136261.

23 Ö. Güngör and P. Gürkan, *Arabian J. Chem.*, 2019, **12**, 2244–2256, DOI: 10.1016/j.arabjc.2015.02.009.

24 S. U. Rehman, R. Nawaz and A. Faiz, *Synth. React. Inorg., Met.-Org., Nano-Met. Chem.*, 2012, **42**, 1053–1059, DOI: 10.1080/15533174.2011.614314.

25 M. J. Frisch, G. W. Trucks, H. B. Schlegel, G. E. Scuseria, M. A. Robb, J. R. Cheeseman, G. Scalmani, V. Barone, G. A. Petersson, H. Nakatsuji, X. Li, M. Caricato, A. V. Marenich, J. Bloino, B. G. Janesko, R. Gomperts, B. Mennucci, H. P. Hratchian, J. V. Ortiz, A. F. Izmaylov, J. L. Sonnenberg, D. Williams-Young, F. Ding, F. Lipparini, F. Egidi, J. Goings, B. Peng, A. Petrone, T. Henderson, D. Ranasinghe, V. G. Zakrzewski, J. Gao, N. Rega, G. Zheng, W. Liang, M. Hada, M. Ehara, K. Toyota, R. Fukuda, J. Hasegawa, M. Ishida, T. Nakajima, Y. Honda, O. Kitao, H. Nakai, T. Vreven, K. Throssell, J. A. Montgomery, Jr., J. E. Peralta, F. Ogliaro, M. J. Bearpark, J. J. Heyd, E. N. Brothers, K. N. Kudin, V. N. Staroverov, T. A. Keith, R. Kobayashi, J. Normand, K. Raghavachari, A. P. Rendell, J. C. Burant, S. S. Iyengar, J. Tomasi, M. Cossi, J. M. Millam, M. Klene, C. Adamo, R. Cammi, J. W. Ochterski, R. L. Martin, K. Morokuma, O. Farkas, J. B. Foresman and D. J. Fox, *Gaussian 16, Revision C.01*, Gaussian, Inc., Wallingford CT, 2016.

26 S. Ahsen, I. Tanvir, N. Uddin, T. Yasmeen, S. Abbas, S. Naz, A. Haider, S. Bhattacharya, U. Kortz, F. Rashid, J. Iqbal and S. Ali, *Inorg. Chim. Acta*, 2024, **564**, 121965, DOI: 10.1016/j.ica.2024.121965.

27 A. Fetoh, K. A. Asla, A. A. El-Sherif, H. El-Didamony and G. M. Abu El-Reash, *J. Mol. Struct.*, 2019, **1178**, 524–537, DOI: 10.1016/j.molstruc.2018.10.066.

28 A. Mederos, S. Dominguez, R. Hernandez-Molina, J. Sanchiz and F. Brito, *Coord. Chem. Rev.*, 1999, **193–195**, 857–911.

29 A. A. El-Sherif and M. S. Aljahdali, *J. Coord. Chem.*, 2013, **66**, 3423–3468, DOI: 10.1080/00958972.2013.839027.

30 H. Joshi, F. S. Kamounah, C. Gooijer, G. van der Zwan and L. Antonov, *J. Photochem. Photobiol., A*, 2002, **152**, 183–191.

31 S. R. Salman and F. S. Kamounah, *Spectrosc. Lett.*, 2002, **35**, 327–335.

32 R. Chandra, A. K. Manna, M. Sahu, K. Rout and G. K. Patra, *Inorg. Chim. Acta*, 2020, **499**, 119192, DOI: 10.1016/j.ica.2019.119192.

33 B. Samanta, J. Chakraborty, S. Shit, S. R. Batten, P. Jensen, J. D. Masuda and S. Mitra, *Inorg. Chim. Acta*, 2007, **360**, 2471–2484, DOI: 10.1016/j.ica.2006.12.019.

34 M. Kumar, A. K. Singh, A. K. Singh, R. K. Yadav, S. Singh, A. P. Singh and A. Chauhan, *Coord. Chem. Rev.*, 2023, **488**, 215176, DOI: 10.1016/j.ccr.2023.215176.

35 C. P. Matos, Y. Addis, P. Nunes, S. Barroso, I. Alho, M. Martins, A. P. A. Matos, F. Marques, I. Cavaco, J. C. Pessoa and I. Correia, *J. Inorg. Biochem.*, 2019, **198**, 110727, DOI: 10.1016/j.jinorgbio.2019.110727.

36 N. Ghobadi, *Int. Nano Lett.*, 2013, **3**, 2–4, DOI: 10.1186/2228-5326-3-2.

37 K. Mariselvam and J. Liu, *Opt. Mater.*, 2021, **114**, 110997, DOI: 10.1016/j.optmat.2021.110997.

38 Ö. B. Mergen and E. Arda, *Synth. Met.*, 2020, **269**, 116539, DOI: 10.1016/j.synthmet.2020.116539.

39 I. Kaya, B. Ayten and D. Şenol, *Opt. Mater.*, 2018, **78**, 421–431, DOI: 10.1016/j.optmat.2018.02.057.

40 J. P. Wu, Y. C. Cheng, L. Lu, J. Wang and S. B. Qiao, *Acta Crystallogr., Sect. C: Cryst. Struct. Commun.*, 2021, **C77**, 257–261, DOI: 10.1107/S2053229621004642.

41 E. N. Nuraneeva, G. B. Guseva, E. V. Antina, M. B. Berezin and A. I. V'yugin, *J. Lumin.*, 2016, **170**, 248–254, DOI: 10.1016/j.jlumin.2015.10.061.

42 T. Wang, Q. Pang, Z. Tong, M. Wang and N. Xiao, *Spectrochim. Acta, Part A*, 2021, **250**, 119249, DOI: 10.1016/j.saa.2020.119249.

43 M. Mukhopadhyay, D. Banerjee, A. Koll, A. Filarowski and S. Mukherjee, *Spectrochim. Acta, Part A*, 2005, **62**, 126–131, DOI: 10.1016/j.saa.2004.12.015.

44 Y. P. Huo, S. Z. Zhu and S. Hu, *Tetrahedron*, 2010, **66**, 8635–8640, DOI: 10.1016/j.tet.2010.09.039.

45 P. Mohanty, R. Behura, V. Bhardwaj, P. P. Dash, S. K. Sahoo and B. R. Jali, *Trends Environ. Anal. Chem.*, 2022, **34**, e00166, DOI: 10.1016/j.teac.2022.e00166.

46 X. Ma, W. Chi, X. Han, C. Wang, S. Liu, X. Liu and J. Yin, *Chin. Chem. Lett.*, 2021, **32**, 1790–1794, DOI: 10.1016/j.cclet.2020.12.031.

47 X. Liu, Y. Sun, Y. Gao, X. Zhang, X. Li, W. Zheng, M. Liu, T. Zhao, X. A. Yuan, M. Yue and Z. Liu, *J. Inorg. Biochem.*, 2025, **262**, 112767, DOI: 10.1016/j.jinorgbio.2024.112767.

48 K. Ogawa and J. Harada, *J. Mol. Struct.*, 2003, **647**, 211–216, DOI: 10.1016/S0022-2860(02)00526-4.

49 A. Ohshima, A. Momotake and T. Arai, *J. Photochem. Photobiol., A*, 2004, **162**, 473–479, DOI: 10.1016/S1010-6030(03)00388-5.

50 N. Klinhom, N. Saengsuwan, S. Sriyab, P. Prompinit, S. Hannongbua and S. Suramitr, *Spectrochim. Acta, Part A*, 2019, **206**, 359–366, DOI: 10.1016/j.saa.2018.08.010.

51 V. I. Minkin, A. V. Tsukanov, A. D. Dubonosov and V. A. Bren, *J. Mol. Struct.*, 2011, **998**, 179–191, DOI: 10.1016/j.molstruc.2011.05.029.

52 Y. Zhao, K. Chen, B. Yu, Q. Wan, Y. Wang, F. Tang and X. Li, *J. Mol. Struct.*, 2024, **1317**, 139126, DOI: 10.1016/j.molstruc.2024.139126.

53 T. Jiang, Y. Fan, J. H. Lu, C. Huang and B. X. Zhu, *Spectrochim. Acta, Part A*, 2024, **322**, 124827, DOI: 10.1016/j.saa.2024.124827.

54 M. J. Tian, H. Q. Tian, T. Jiang, H. H. Yu, C. Huang, B. X. Zhu and C. Zhu, *Tetrahedron*, 2024, **167**, 134288, DOI: 10.1016/j.tet.2024.134288.

55 G. Zhang, S. Yu, J. Peng, Y. Xiong, L. Hu and W. Lai, *Trends Anal. Chem.*, 2025, **183**, 118098, DOI: 10.1016/j.trac.2024.118098.

56 J. J. Shao, J. L. Ni, Y. Liang, X. D. Xu and F. M. Wang, *J. Mol. Struct.*, 2021, **1244**, 130975, DOI: 10.1016/j.molstruc.2021.130975.

57 D. Majumdar, S. Dey, D. Das, D. K. Singh, S. Das, K. Bankura and D. Mishra, *J. Mol. Struct.*, 2019, **1185**, 112–120, DOI: 10.1016/j.molstruc.2019.02.092.

58 A. He, C. Zhong, H. Huang, Y. Zhou, Y. He and H. Zhang, *J. Lumin.*, 2008, **128**, 1291–1296, DOI: 10.1016/j.jlumin.2007.12.031.

59 E. Liu, Y. Zhuo Zhang, J. Tan, C. Yang, L. Li, J. A. Golen, A. L. Rheingold and G. Zhang, *Polyhedron*, 2015, **102**, 41–47, DOI: 10.1016/j.poly.2015.07.074.

60 C. Anitha, C. D. Sheela, P. Tharmaraj and S. J. Raja, *Spectrochim. Acta, Part A*, 2012, **98**, 35–42, DOI: 10.1016/j.saa.2012.08.022.

61 F. Purtas, K. Sayin, G. Ceyhan, M. Kose and M. Kurtoglu, *J. Mol. Struct.*, 2017, **1137**, 461–475, DOI: 10.1016/j.molstruc.2017.02.065.

62 Ya. N. Albrekht, V. F. Plyusnin, E. M. Glebov, M. S. Milutka, A. S. Burlov, Y. V. Koshchienko, V. G. Vlasenko, V. A. Lazarenko and L. D. Popov, *J. Lumin.*, 2024, **266**, 120286, DOI: 10.1016/j.jlumin.2023.120286.

63 N. Ahmad and R. Shirin, *Iran. J. Chem. Chem. Eng.*, 2019, **38**, 79–90.

64 S. Z. Zhang, G. Guo, W. M. Ding, J. Li, Y. Wu, H. J. Zhang, J. Q. Guo and Y. X. Sun, *J. Mol. Struct.*, 2021, **1230**, 129627, DOI: 10.1016/j.molstruc.2020.129627.

65 M. Liu, H. Yang, D. Li, Q. Yao, H. Wang, Z. Zhang and J. Dou, *Inorg. Chim. Acta*, 2021, **522**, 120384, DOI: 10.1016/j.ica.2021.120384.

66 J. Cao, Z. Jia, W. Chen, Y. Song, Z. Yu, Y. Dong and Y. Ren, *Inorg. Chim. Acta*, 2025, **577**, 122494, DOI: 10.1016/j.ica.2024.122494.

67 J. Dong, T. Wan, K. Li, X. Kong, Q. Shen and H. Wu, *J. Mol. Struct.*, 2022, **1264**, 133340, DOI: 10.1016/j.molstruc.2022.133340.

68 S. Dalbera, S. S. Saha, H. A. Sparkes and S. Mohanta, *J. Mol. Struct.*, 2025, **1319**, 139537, DOI: 10.1016/j.molstruc.2024.139537.

69 H. Pyngrope, J. Chetia, B. Kharpan, R. Nandi, A. K. Pradhan, P. C. Paul, H. A. R. Pramanik and D. Kumar, *Inorg. Chem. Commun.*, 2025, **173**, 113770, DOI: 10.1016/j.inoche.2024.113770.

70 G. Keser Karaoğlan, *J. Mol. Struct.*, 2022, **1256**, 132534, DOI: 10.1016/j.molstruc.2022.132534.

71 E. H. H. Hasabeldaim, H. C. Swart and R. E. Kroon, *RSC Adv.*, 2023, **13**, 5353–5366, DOI: 10.1039/d2ra07897j.

72 C. C. Vidyasagar, B. M. Muñoz Flores, V. M. Jiménez-Pérez and P. M. Gurubasavaraj, *Mater. Today Chem.*, 2019, **11**, 133–155, DOI: 10.1016/j.mtchem.2018.09.010.

73 F. S. M. Canisares, A. G. Bispo-Jr, A. M. Pires and S. A. M. Lima, *Optik*, 2020, **219**, 164995, DOI: 10.1016/j.ijleo.2020.164995.

74 L. E. Lopez-Ruiz, Ch. J. Salas-Juárez, I. Garduño-Wilches, H. I. Beltran, U. Orozco-Valencia, R. I. López-Esquivel, J. C. Guzman-Olguin, M. Centeno-Alvarez and J. Guzman-Mendoza, *J. Lumin.*, 2023, **263**, 120020, DOI: 10.1016/j.jlumin.2023.120020.

75 N. Ganji, A. Rambabu, N. Vamsikrishna, S. Daravath and Shivaraj, *J. Mol. Struct.*, 2018, **1173**, 173–182, DOI: 10.1016/j.molstruc.2018.06.100.

76 A. Daina, O. Michielin and V. Zoete, *J. Chem. Inf. Model.*, 2014, **54**, 3284–3301, DOI: 10.1021/ci500467k.

77 A. Daina and V. Zoete, *ChemMedChem*, 2016, **11**, 1117–1121, DOI: 10.1002/cmdc.201600182.

78 Z. H. Chohan, S. H. Sumrra, M. H. Youssoufi and T. B. Hadda, *Eur. J. Med. Chem.*, 2010, **45**, 2739–2747, DOI: 10.1016/j.ejmech.2010.02.053.

79 A. Daina, O. Michielin and V. Zoete, *Sci. Rep.*, 2017, **7**, 42717, DOI: 10.1038/srep42717.